Abstracta

Ano XXVI - N. 04

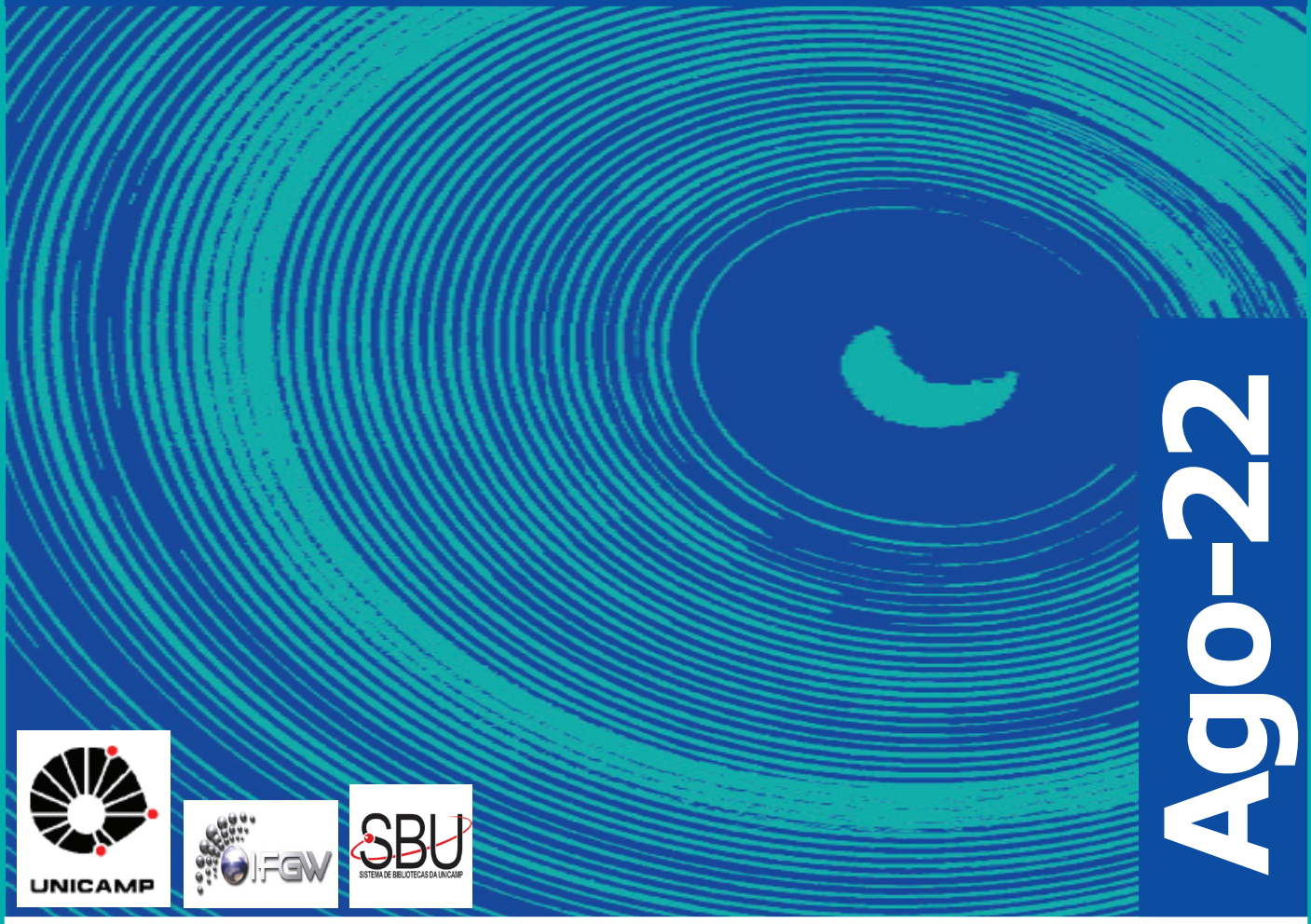

Ago-22

Artigos publicados - P134-2022 à P210-2022

Errata - E001-2022

Capítulo de livro - L001-2022

Defesas de Dissertações do IFGW - D013-2022 à D19-2022

Defesas de Teses do IFGW - T011-2022 à T15-2022

Artigos publicados

[P134-2022] "A Search for Photons with Energies Above 2 x 10(17) eV Using Hybrid Data from the Low-Energy Extensions of the Pierre Auger Observatory"

Abreu, P.; Aglietta, M.; **Arbeletche, L. B.*; Chinellato, J. A.*; Franco, D. de O.*; Dobrigkeit, C.*; Fauth, A. C.*; Payeras, A. M.*; Muller, M. A.***; et al. Pierre Auger Collaboration

Ultra-high-energy photons with energies exceeding 10(17) eV offer a wealth of connections to different aspects of cosmic-ray astrophysics as well as to gamma-ray and neutrino astronomy. The recent observations of photons with energies in the 10(15) eV range further motivate searches for even higher-energy photons. In this paper, we present a search for photons with energies exceeding 2 x 10(17) eV using about 5.5 yr of hybrid data from the low-energy extensions of the Pierre Auger Observatory. The upper limits on the integral photon flux derived here are the most stringent ones to date in the energy region between 10(17) and 10(18) eV.

ASTROPHYSICAL JOURNAL 933[2], 125, 2022. DOI: 10.3847/1538-4357/ac7393 2022

[P135-2022] "Adhesion of Amorphous Carbon Nanofilms on Ferrous Alloy Substrates Using a Nanoscale Silicon Interlayer: Implications for Solid-State Lubrication"

Boeira, C. D.; **Cemin, F.***; Leidens, L. M.; Weber, J. S.; Michels, A. F.; Aguzzoli, C.; Serra, R.; Evaristo, M.; Fernandes, F.; **Alvarez, F.***; Cavaleiro, A.; Figueroa, C. A.

The low adhesion of amorphous carbon (a-C) films on ferrous alloys has restricted massive industrial application since their development, restricting application to mechanical and electromechanical components. Although different mechanisms have been raised to describe the a-C film adhesion, the chemical affinity and the role of oxygen at the interfaces are the key issue. Nevertheless, a quantitative approach considering the oxygen adsorption and the adhesion strength/base pressure relationship is still not proposed, which would be of special interest in industry. In this study, we analyze the influence of the base pressure on the adhesion of amorphous carbon (a-C) films onto a ferrous alloy intermediated by a nanometric silicon interlayer. The different base pressure deposition resulted in different adhesion of the films. By means of structural and chemical techniques, the oxygen content at the interfaces was quantified and correlated with the base pressure before thin film deposition. We propose a quantitative physicochemical model that correlates the a-C film adhesion with oxygen located at the interfaces, which is indirect evidence of its previous presence in the deposition chamber, as a fraction of the residual gases from the base pressure. As adhesion depends on oxygen content, we used the Langmuir isothermal law to evaluate this dependence with good agreement. This model may be of potential interest in plasma surface engineering and process automatization not only for carbon-related materials deposited on metals, mainly in its potential use as a solid lubricant.

ACS APPLIED NANO MATERIALS 5[3], 3763-3772, 2022. DOI: 10.1021/acsanm.1c04429

[P136-2022] "Analysis of the CP structure of the Yukawa coupling between the Higgs boson and tau leptons in proton-proton collisions at root s=13 TeV"

Tumasyan, A.; Adam, W.; **Chinellato, J. A.***; et al. CMS Collaboration

The first measurement of the CP structure of the Yukawa coupling between the Higgs boson and tau leptons is presented. The measurement is based on data collected in proton-proton collisions at root s = 13 TeV by the CMS detector at the LHC, corresponding to an integrated luminosity of 137 fb(-1). The analysis uses the angular correlation between the decay planes of tau leptons produced in Higgs boson decays. The effective mixing angle between CP-even and CP-odd tau Yukawa couplings is found to be -1 +/- 19 degrees, compared to an expected value of 0 +/- 21 degrees at the 68.3% confidence level. The data disfavour the pure CP-odd scenario at 3.0 standard deviations. The results are compatible with predictions for the standard model Higgs boson.

JOURNAL OF HIGH ENERGY PHYSICS [6], 012, 2022. DOI: 10.1007/JHEP06(2022)012

[P137-2022] "Assessing the performance of quantum annealing with nonlinear driving"

Soriani, A.*; Naze, P.*; Bonanca, M. V. S.*; Gardas, B.; **Deffner, S.***

Current-generation quantum annealers have already proven to be successful problem solvers. Yet quantum annealing is still very much in its infancy, with suboptimal applicability. For instance, to date it is still an open question which annealing protocol causes the fewest diabatic excitations for a given eigenspectrum, and even whether there is a universally optimal strategy. Therefore, in this paper, we report analytical and numerical studies of the diabatic excitations arising from nonlinear protocols applied to the transverse field Ising chain, the exactly solvable model that serves as a quantum annealing playground. Our analysis focuses on several driving schemes that inhibit or facilitate the dynamic phases discussed in a previous work. Rather remarkably, we find that the paradigmatic Kibble-Zurek behavior can be suppressed with ???pauses??? in the evolution, both for crossing and for stopping at the quantum critical point of the system.

PHYSICAL REVIEW A 105[5], 052442, 2022. DOI: 10.1103/PhysRevA.105.052442

[P138-2022] "Constraints on heavy neutral leptons interacting with a singlet scalar"

Cline, J. M.; **Gambini, G.***

Heavy neutral leptons (HNLs) are an attractive minimal extension of the Standard Model, as is a singlet scalar s mixing with the Higgs boson. If both are present, it is natural for HNLs to interact with s. For a light singlet, the decay N -> s nu can dominate over weak HNL decays. We reinterpret existing constraints on HNL mixing from the DELPHI, CHARM, and Belle experiments for 0.5-100 GeV mass HNLs, taking into account the new decay channel. Although the constraints are typically weakened, in some cases they can become stronger, due to observable s -> l(+) l(-) decays in the detectors. The method presented here could be used to recast constraints from other (older) experiments without resorting to computationally expensive Monte Carlo simulations. In addition, we update and correct some errors in the analysis of the original constraints, in the absence of the singlet.

PHYSICAL REVIEW D 105[11], 115035, 2022. DOI: 10.1103/PhysRevD.105.115035

[P139-2022] "Cross-correlation of Dark Energy Survey Year 3 lensing data with ACT and Planck thermal Sunyaev-Zel'dovich effect observations. I. Measurements, systematics tests, and feedback model constraints"

Gatti, M.; Pandey, S.; **Alsina, A. N.***; et al. DES ACT Collaboration

We present a tomographic measurement of the cross-correlation between thermal Sunyaev-Zel'dovich (TSZ) maps from Planck and the Atacama Cosmology Telescope and weak galaxy lensing shears measured during the first three years of observations of the Dark Energy Survey. This correlation is sensitive to the thermal energy in baryons over a wide redshift range and is therefore a powerful probe of astrophysical feedback. We detect the correlation at a statistical significance of 21 sigma, the highest significance to date. We examine the TSZ maps for potential contaminants, including cosmic infrared background and radio sources, finding that cosmic infrared background has a substantial impact on our measurements and must be taken into account in our analysis. We use the cross-correlation measurements to test different feedback models. In particular, we model the TSZ using several different pressure profile models calibrated against hydrodynamical simulations. Our analysis marginalizes over redshift uncertainties, shear calibration biases, and intrinsic alignment effects. We also marginalize over Omega(m) and sigma(8) using Planck or DES priors. We find that the data prefer the model with a low amplitude of the pressure profile at small scales, compatible with a scenario with strong active galactic nuclei feedback and ejection of gas from the inner part of the halos. When using a more flexible model for the shear profile, constraints are weaker, and the data cannot discriminate between different baryonic prescriptions.

PHYSICAL REVIEW D 105[12], 123525, 2022. DOI: 10.1103/PhysRevD.105.123525

[P140-2022] "Cross-correlation of Dark Energy Survey Year 3 lensing data with ACT and Planck thermal Sunyaev--Zel'dovich effect observations. II. Modeling and constraints on halo pressure profiles"

Pandey, S.; Gatti, M.; **Alsina, A. N.***; et al. DES & ACT Collaboration

Hot, ionized gas leaves an imprint on the cosmic microwave background via the thermal Sunyaev-Zel'dovich (tSZ) effect. The cross-correlation of gravitational lensing (which traces the projected mass) with the tSZ effect (which traces the projected gas pressure) is a powerful probe of the thermal state of ionized baryons throughout the Universe and is sensitive to effects such as baryonic feedback. In a companion paper (Gatti et al. Phys. Rev. D 105, 123525 (2022)), we present tomographic measurements and validation tests of the cross-correlation between Galaxy shear measurements from the first three years of observations of the Dark Energy Survey and tSZ measurements from a combination of Atacama Cosmology Telescope and Planck observations. In this work, we use the same measurements to constrain models for the pressure profiles of halos across a wide range of halo mass and redshift. We find evidence for reduced pressure in low-mass halos, consistent with predictions for the effects of feedback from active Galactic nuclei. We infer the hydrostatic mass bias (B equivalent to M-500c/M-SZ) from our measurements, finding B = 1.8 +/- 0.1 when adopting the Planck-preferred cosmological parameters. We additionally find that our measurements are consistent with a nonzero redshift evolution of B, with the correct sign and sufficient magnitude to explain the mass bias necessary to reconcile cluster count measurements with the Planck-preferred cosmology. Our analysis introduces a model for the impact of intrinsic alignments (IAs) of galaxy shapes on the shear-tSZ correlation. We show that IA can have a significant impact on these correlations at current noise levels.

PHYSICAL REVIEW D 105[12], 123526, 2022. DOI: 10.1103/PhysRevD.105.123526

[P141-2022] "Dark Energy Survey Year 3 results: Exploiting small-scale information with lensing shear ratios"

Sanchez, C.; Prat, J.; **Alsina, A. N.***; et al. DES Collaboration

Using the first three years of data from the Dark Energy Survey (DES), we use ratios of small-scale galaxy-galaxy lensing measurements around the same lens sample to constrain source redshift uncertainties, intrinsic alignments and other systematics or nuisance parameters of our model. Instead of using a simple geometric approach for the ratios as has been done in the past, we use the full modeling of the galaxy-galaxy lensing measurements, including the corresponding integration over the power spectrum and the contributions from intrinsic alignments and lens magnification. We perform extensive testing of the small--scale shear-ratio (SR) modeling by studying the impact of different effects such as the inclusion of baryonic physics, nonlinear biasing, halo occupation distribution descriptions and lens magnification, among others, and using realistic N-body simulations of the DES data. We validate the robustness of our constraints in the data by using two independent lens samples with different galaxy properties, and by deriving constraints using the corresponding large-scale ratios for which the modeling is simpler. The results applied to the DES Y3 data demonstrate how the ratios provide significant improvements in constraining power for several nuisance parameters in our model, especially on source redshift calibration and intrinsic alignments. For source redshifts, SR improves the constraints from the prior by up to 38% in some redshift bins. Such improvements, and especially the constraints it provides on intrinsic alignments, translate to tighter cosmological constraints when shear ratios are combined with cosmic shear and other 2pt functions. In particular, for the DES Y3 data, SR improves S-8 constraints from cosmic shear by up to 31%, and for the full combination of probes (3 x 2pt) by up to 10%. The shear ratios presented in this work are used as an additional likelihood for cosmic shear, 2 x 2pt and the full 3 x 2pt in the fiducial DES Y3 cosmological analysis.

PHYSICAL REVIEW D 105[8], 083529, 2022. DOI: 10.1103/PhysRevD.105.083529

[P142-2022] "Dark energy survey year 3 results: High-precision measurement and modeling of galaxy-galaxy lensing"

Prat, J.; Blazek, J.; **Alsina, A. N.***; et al. DES Collaboration

We present and characterize the galaxy-galaxy lensing signal measured using the first three years of data from the Dark Energy Survey (DES Y3) covering 4132 deg2. These galaxy-galaxy measurements are used in the DES Y3 3 ?? 2 pt cosmological analysis, which combines weak lensing and galaxy clustering information. We use two lens samples: a magnitude-limited sample and the redMaGiC sample, which span the redshift range-0.2???1 with 10.7 and 2.6 M galaxies, respectively. For the source catalog, we use the METACALIBRATION shape sample, consisting of <^>-100 M galaxies separated into four tomographic bins. Our galaxy-galaxy lensing estimator is the mean tangential shear, for which we obtain a total SNR of-148 for MagLim (-120 for redMaGiC), and-67 (-55) after applying the scale cuts of 6 Mpc=h. Thus we reach percent-level statistical precision, which requires that our modeling and systematic-error control be of comparable accuracy. The tangential shear model used in the 3 ?? 2 pt cosmological analysis includes lens magnification, a five-parameter intrinsic alignment model, marginalization over a point mass to remove information from small scales and a linear galaxy bias model validated with higher-order terms. We explore the impact of these choices on the tangential shear observable and study the significance of effects not included in our model, such as reduced shear, source magnification, and source clustering. We also test the robustness of our measurements to various observational and systematics effects, such as the impact of observing conditions, lens-source clustering, random-point subtraction, scale-dependent METACALIBRA--TION responses, point spread function residuals, and B modes.

PHYSICAL REVIEW D 105[8], 083528, 2022. DOI: 10.1103/PhysRevD.105.083528

[P143-2022] "Dark Energy Survey Year 3 Results: Three--point shear correlations and mass aperture moments"

Secco, L. F.; Jarvis, M.; **Alsina, A. N.***; et al.

We present high signal-to-noise measurements of three-point shear correlations and the third moment of the mass aperture statistic using the first 3 years of data from the Dark Energy Survey. We additionally obtain the first measurements of the configuration and scale dependence of the four three-point shear correlations which carry cosmological information. With the third-order mass aperture statistic, we present tomographic measurements over angular scales of 4 to 60 arcminutes with a combined statistical significance of 15.0??. Using the tomographic information and measuring also the second-order mass aperture, we additionally obtain a skewness parameter and its redshift evolution. We find that the amplitudes and scale-dependence of these shear 3pt functions are in qualitative agreement with measurements in a mock galaxy catalog based on N-body simulations, indicating promise for including them in future cosmological analyses. We validate our measurements by showing that B-modes, parity-violating contributions and PSF modeling uncertainties are negligible, and determine that the measured signals are likely to be of astrophysical and gravitational origin.

PHYSICAL REVIEW D 105[10], 103537, 2022. DOI: 10.1103/PhysRevD.105.103537

[P144-2022] "Determination of the effective anisotropy of magnetite/maghemite nanoparticles from Mossbauer effect spectra"

Orozco-Henao, J. M.; **Muraca, D.***; Sanchez, F. H.; Zelis, P. M.

The stoichiometry and the effective anisotropy constant (K--eff) of several samples of iron-oxide nanoparticles with sizes between 12 and 51 nm, showing spheroidal and cubic shapes, were studied by means of Mossbauer spectroscopy at room temperature (RT). Mossbauer spectra were analyzed and fitted considering two magnetically split subspectra due to Fe3+ and Fe2.5+ ions in tetrahedral and octahedral sites of a non--stoichiometric magnetite, respectively. In order to take into account the collective fluctuations of the NPs magnetic moments, the measured Mossbauer spectra were fitted including a distribution of the hyperfine interactions associated with the NPs volume (V) distribution. To determine the K-eff value, a direct comparison between the size distribution obtained from structural characterization techniques and the KeffV product obtained from Mossbauer spectra fitting was made. In this regard, the K-eff value was determined as the one that maximizes the coincidence between the mean NPs sizes obtained by both methods. Finally, an overall surface anisotropy constant K-s value was obtained by means of a linear relation between the mean NP size, the experimentally determined K-eff and a weighted arithmetic mean magnetic anisotropy related with the bulk magnetite and maghemite anisotropy constants at RT. An evident relation between the KeffV values through the parameter lambda = KeffV/k(B)T and the magnetite/maghemite fraction in each sample was also observed.

JOURNAL OF PHYSICS D-APPLIED PHYSICS 55[33], 335302, 2022. DOI: 10.1088/1361-6463/ac708e

[P145-2022] "Effect of stabilization and fatty acids chain length on the crystallization behavior of interesterified blends during storage"

Silva, M. G. da; Godoi, K. R. R. de; **Cardoso, L. P.*;** Ribeiro, A. P. B.

In this work, we studied the influence of fatty acid chain length and crystallization temperature on the crystallization behavior during the storage of binary blends modified by chemical interesterification. The blends were produced with soybean oil and fully hydrogenated oils from palm kernel, palm, soybean, microalgae, and crambe, evaluated separately, at a ratio of 50:50 (% w/w). The blends were crystallized by two crystalline stabilization methods. In method I, the samples were maintained at 25 ? for 24 h before the analyses. In method II, the samples were maintained at 5 ? for 24 h, followed by crystalline stabilization at 25 ? for 24 h before the analyses. The interesterification reaction caused considerable changes in the TAGs profile with increasing asymmetric TAGs. These TAGs changes promoted an increase in the crystallization induction time, a decrease in the maximum solids content, and changes in crystals morphology. The increase in the FAs chain length promoted the increased nucleation rate that influenced morphology crystals. Method II promoted a reduction in the me-dium diameter of crystals and the appearance of the 13 phase with storage time. For crystallization carried out at higher temperatures (method I), we observed that 13' was favored. Unusual polymorphic transitions were observed with storage time in samples with higher tristearin content. We identified clear correlations between the predominance of 13' phase in the interesterified blends and TAGs of S2U and SU2-type. In addition, the blends with a more diverse range of fatty acids concerning chain size also showed the 13' polymorph. 13 polymorph, on the other hand, was associated with symmetric TAGs, S3 and U3, and CN-54 type TAG. In this study, we used the Rietveld method to quantify the polymorphs and amorphous content in the blends before and after the randomization reaction. This approach allowed a deeper understanding of the crystalline behavior in the blends, which would be difficult to achieve by performing only a visual analysis of the X-ray diffractograms.

FOOD RESEARCH INTERNATIONAL 157, 111208, 2022. DOI: 10.1016/j.foodres.2022.111208

[P146-2022] "Effects of Ca2+ -> Mg2+ substitution on the properties of cementitious tobermorite"

Rego, J. S.*; Miranda, C. R.; **Koning, M. de***

Using density-functional-theory calculations we assess the effects of the isovalent Ca2+ -> Mg2+ substitutions on the mineral structure of tobermorite, a major analog of the main hydrated cement phase, calcium-silicate-hydrate (CSH). From the structural point of view, due to its smaller ionic radius, Mg substitution leads to an overall decrease of the lattice parameters for the 9 angstrom (dry) and 11 angstrom (hydrated) tobermorite structures used in the study. Furthermore, Mg doping at intralayer sites leads to a considerable distortion of the unit cell due to a changing oxygen coordination number. With the increasing amount of Mg doping, chemical bond analysis shows an overall increase in the bond strength with the crystal cohesion enhancement. In addition, Mg sites in the dry and hydrated tobermorite are characterized by an enhanced reactivity, which may be useful in capturing CO2. With regard to the elastic properties, Mg doping leads to an overall stiffening of the elastic moduli. However, depending on the particular site, Mg doping may give rise to an increased elastic anisotropy. Overall, the present results indicate that Mg-based tobermorite structures may be useful prospects in the search for alternative components toward the development of high-performance, environmentally friendly cementitious materials.

PHYSICAL REVIEW MATERIALS 6[6], 063604, 2022. DOI: 10.1103/PhysRevMaterials.6.063604

[P147-2022] "Effects of external pressure on the narrow--gap semiconductor Ce3Cd2As6"

Piva, M. M.*; Xiang, L.; Thompson, J. D.; Bud'ko, S. L.; Ribeiro, R. A.; Canfield, P. C.; Rosa, P. F. S.

Here we report the magnetic and electronic properties of recently discovered Ce3Cd2As6. At ambient pressure, Ce3Cd2As6 presents a semiconducting behavior with an activation gap of 74(1) meV. At 136 K, a sudden increase of the electrical resistivity and a peak in specific heat are consistent with a charge density wave transition. At low temperatures, antiferromagnetic order of the Ce3+ ions occurs below T-N = 4.0 K with a magnetic hard axis along the c axis and a Gamma(6) = vertical bar +/- 1/2 > doublet ground state. The application of external pressure strongly suppresses the charge density wave order, which is completely suppressed above 0.8(1) GPa, and induces a metallic ground state. No evidence for superconductivity is detected above 2 K. Conversely, the antiferromagnetic state is favored by pressure, reaching a transition temperature of 5.3 K at 3.8(1) GPa. Notably, the resistivity anomaly characterizing the antiferromagnetic order changes with increasing pressure, indicating that two different magnetic phases might be present in Ce3Cd2As6 under pressure. This change in ordering appears to be associated to the crossing of the T-CDW and T-N lines.

PHYSICAL REVIEW B 105[9], 094443, 2022. DOI: 10.1103/PhysRevB.105.094443

[P148-2022] "Electron response to radiation under linear acceleration: Classical, QED, and accelerated frame predictions"

Hegelich, B. M.; Labun, L.; Labun, O. Z.; **Torrieri, G.*; Truran, H.***

A model detector undergoing constant, infinite-duration acceleration converges to an equilibrium state described by the Hawking-Unruh temperature T-a = (a/2 pi)(h/c). To relate this prediction to experimental observables, a pointlike charged particle, such as an electron, is considered in place of the model detector. Instead of the detector's internal degree of freedom, the electron's low-momentum fluctuations in the plane transverse to the acceleration provide a degree of freedom and observables which are compatible with the symmetry and thermalize by interaction with the radiation field. General arguments in the accelerated frame suggest thermalization and a fluctuation-dissipation relation but leave underdetermined the magnitude of either the fluctuation or the dissipation. Lab frame analysis reproduces the radiation losses, described by the classical Lorentz-Abraham-Dirac equation, and reveals a classical stochastic force. We derive the fluctuation-dissipation relation between the radiation losses and stochastic force as well as equipartition (p(perpendicular to)(2)) = 2mT(a) from classical electrodynamics alone. The derivation uses only straightforward statistical definitions to obtain the dissipation and fluctuation dynamics. Since high accelerations are necessary for these dynamics to become important, we compare classical results for the relaxation and diffusion times to strong-field quantum electrodynamics results. We find that experimental realization will require development of more precise observables. Even wakefield accelerators, which offer the largest linear accelerations available in the lab, will require improvement over current technology as well as high statistics to distinguish an effect.

PHYSICAL REVIEW D 105[9], 096034, 2022. DOI: 10.1103/PhysRevD.105.096034

[P149-2022] "Enhancing the measurement range of laser speckle systems"

Cabral, T. D.*; Cordeiro, C. M. B.*; Fujiwara, E.

Laser speckle-based systems provide sensitive measurements of displacement and stain. However, the typical saturation of correlation functions restricts the application of such techniques regarding their dynamic range. Therefore, this paper proposes using the extended zero-mean normalized cross-correlation (EZNCC) algorithm to automatically update the reference speckle image according to a programmable threshold, allowing for exceeding the decorrelation limit. Experiments investigated the effect of rigid body displacements and thermal strain at the light scattering surface (a ceramic container). The EZNCC yielded similar to 30 mu m resolution over a continuous 1500 mu m range for displacement measurements, and similar to 0.2 degrees C resolution between 21.5 degrees C and 61.5 degrees C for the temperature analysis. As this method requires minor updates to the traditional correlation algorithms, the ENZCC does not require modifications to the optical setups, improving the dynamic range and ensuring the high sensitivity of speckle correlation systems in a feasible, straightforward approach.

MICROWAVE AND OPTICAL TECHNOLOGY LETTERS, 2022. DOI: 10.1002/mop.33388, **Primeira data de acesso:** JUN 2022

[P150-2022] "Exchange interaction between localized magnetic moments and conduction-electrons in Er doped gold nanoparticles synthesized by laser ablation in water"

Fabris, F.*; Garcia-Flores, A. F.*; Urbano, R. R.*; Rettori, C.*

In this work, we report a fundamental study on the exchange interaction between localized rare earth magnetic moments and conduction electrons of Er3+ diluted in Au metallic nanoparticles (NPs) produced by laser ablation in liquid. The study was carried out in Au1-xErx (x & LE; 0.026) bulk metallic alloys and NPs with a mean size of 20 nm. The samples were characterized by means of x-ray diffraction, transmission electron microscopy, magnetic susceptibility, and electron spin resonance (ESR) experiments. The obtained results showed that, despite the high temperature and being far away from chemical equilibrium throughout the laser ablation process, in the AuNPs, the Er3+ (J = 15/2) ground state of the crystal electric field split multiplet remains a & UGamma;(7) (g = 6.79) Kramers doublet with the expected g-shift and T-dependence of the ESR linewidth, preserving the general bulk properties and the cubic symmetry. In addition, the Au1-xErx NPs present narrow ESR residual linewidth suggesting homogeneous Er3+ doping and negligible strain distribution in the Au1-xErx NPs. This new methodology may certainly provide relevant insight into the study of the intrinsic physical properties of dilute rare earth metallic alloys at the nanometer scale seeking quantum size effects and motivates novel technological applications.

JOURNAL OF APPLIED PHYSICS 131[21], 213903, 2022. DOI: 10.1063/5.0089296

[P151-2022] "Exploration of the stratosphere with cosmic--ray muons detected underground"

Taricco, C.; Arnone, E.; Rubinetti, S.; Bizzarri, I.; **Kemp, E.*;** et al. LVD Collaboration

Cosmic radiation is a potential additional tool for atmospheric monitoring. High-energy cosmic rays, interacting in the atmosphere, produce secondary particles, the production and propagation of which are ruled by the state of the atmosphere. Atmospheric muons carry information on the stratosphere, as its temperature modulates their intensity. Here, we present a comprehensive investigation of the 24-year series of the muon flux recorded underground with the Large Volume Detector in the Gran Sasso Laboratory in Italy.

Using advanced spectral-analysis methods, we reveal, in addition to the well-known annual cycle, two significant variations with periods of about four and ten years. These two multiannual components, however, are not present in the series of the so--called effective temperature-an average parameter commonly used to describe the entire atmospheric profile in relationship to the detected muon flux-but we find them in the series of the raw temperatures in the lower-stratospheric levels. We show that the weaker multiannual cycles emerge in the temperature series thanks to the dampening of the dominant annual radiative cycle at these levels, which are affected by higher-frequency variability related to transport and wave processes. We also show that the multiannual variations are not typical only of the Gran Sasso area but are present at large scales throughout the Northern Hemisphere. The analysis of the series of the muon flux also reveals evidence of daily to monthly scale variations, especially during the highly variable winter period. Although such short-term modulations are also found in the series of the effective temperature, we show that the variations of the two series are brought to better agreement when considering only specific layers of the atmosphere depending on the event. The amplitudes of the multiannual variations are significantly larger than those expected based on the temperature modulations. Such differences may be due to acknowledged difficulties of the adopted temperature reanalysis dataset to thoroughly represent long-term variability scales, so that long-term modulations in the raw temperature series and, consequently, in the effective temperature record would result as artificially attenuated. The muon flux therefore may be envisaged as a high time-resolution integrated proxy of lower-stratospheric temperatures.

PHYSICAL REVIEW RESEARCH 4[2], 023226, 2022. DOI: 10.1103/PhysRevResearch.4.023226

[P152-2022] "First Search for Exclusive Diphoton Production at High Mass with Tagged Protons in Proton-Proton Collisions at root s=13 TeV"

Tumasyan, A.; Adam, W.; **Chinellato, J. A.***; et al. CMS Collaboration; TOTEM Collaboration

A search for exclusive two-photon production via photon exchange in proton-proton collisions, pp -> p gamma gamma p with intact protons, is presented. The data correspond to an integrated luminosity of 9.4 fb(-1) collected in 2016 using the CMS and TOTEM detectors at a center-of-mass energy of 13 TeVat the LHC. Events are selected with a diphoton invariant mass above 350 GeVand with both protons intact in the final state, to reduce backgrounds from strong interactions. The events of interest are those where the invariant mass and rapidity calculated from the momentum losses of the forward-moving protons match the mass and rapidity of the central, two-photon system. No events are found that satisfy this condition. Interpreting this result in an effective dimension-8 extension of the standard model, the first limits are set on the two anomalous four-photon coupling parameters. If the other parameter is constrained to its standard model value, the limits at 95% confidence level are vertical bar zeta(1)vertical bar < 2.9 x 10(-1)3 GeV-4 and vertical bar zeta(2)vertical bar < 6.0 x 10(-13) GeV-4.

PHYSICAL REVIEW LETTERS 129[1], 011801, 2022. DOI: 10.1103/PhysRevLett.129.011801

[P153-2022] "Fluctuating relativistic dissipative hydrodynamics as a gauge theory"

Dore, T.; Gavassino, L.; Montenegro, D.; Shokri, M.; **Torrieri, G.***

We argue that different formulations of hydrodynamics are related to uncertainties in the definitions of local thermodynamic and hydrodynamic variables. We show that this ambiguity can be resolved by viewing different formulations of hydrodynamics as particular "gauge choices"which lead to the same physical behavior of the system. Using the example of bulk viscosity, we show that Bemfica-Disconzi-Noronha-Kovtun (BDNK) and Israel-Stewart hydrodynamics are particular "gauge choices"of this type, related by a well-defined transformation of thermodynamic and hydrodynamic variables. We argue that this gauge ambiguity is necessary to ascertain the causality of stochastic hydrodynamic evolution and conjecture that it could explain the applicability of hydrodynamics outside its expected regime of validity since far from equilibrium and close to equilibrium may be related through transformations of this type.

ANNALS OF PHYSICS 442, 168902, 2022. DOI: 10.1016/j.aop.2022.168902

[P154-2022] "Forward rapidity J/psi production as a function of charged-particle multiplicity in pp collisions at root s=5.02 and 13 TeV"

Acharya, S.; Adamova, D.; **Chinellato, D. D.*; Guardiano, G. G.*; Jahnke, C.*; Takahashi, J.***; et al. ALICE Collaboration

The production of J/psi is measured as a function of charged--particle multiplicity at forward rapidity in proton-proton (pp) collisions at center-of-mass energies root s = 5.02 and 13 TeV. The J/psi mesons are reconstructed via their decay into dimuons in the rapidity interval (2.5 < y < 4.0), whereas the charged-particle multiplicity density (dN(ch)/d eta) is measured at midrapidity (vertical bar eta vertical bar < 1). The production rate as a function of multiplicity is reported as the ratio of the yield in a given multiplicity interval to the multiplicity-integrated one. This observable shows a linear increase with charged--particle multiplicity normalized to the corresponding average value for inelastic events (dN(ch)/d eta/< dN(ch)/d eta >), at both the colliding energies. Measurements are compared with available ALICE results at midrapidity and theoretical model calculations. First measurement of the mean transverse momentum (< p(T)>) of J/psi in pp collisions exhibits an increasing trend as a function of dN(ch)/d eta/< dN(ch)/d eta > showing a saturation towards high charged-particle multiplicities.

JOURNAL OF HIGH ENERGY PHYSICS [6], 015, 2022. DOI: 10.1007/JHEP06(2022)015

[P155-2022] "Functionalization of the hydroxyapatite surface with ZnO for alizarin immobilization"

Oliveira, C.; Oliveira, A. L. M. de; Chantelle, L.; Cavalcanti, G. R. S.; **Landers, R.***; Medina-Carrasco, S.; Orta, M. D.; Silva, E. C.; Jaber, M.; Fonseca, M. G.

The surface of hydroxyapatite (HAp) was functionalized by the deposition of ZnO using microwave-assisted co precipitation and hydrothermal synthesis with sucrose as a template. X-ray diffraction indicated the formation of ZnO/Zn-HAps without a significant change in the crystallinity of HAp. X-ray photoelectron spectroscopy indicated the substitution of Ca2+ by Zn2+ in the HAp structure and the formation of ZnO/Zn-HAp-type compounds, corroborating the refinement data. The morphology of the prepared particles was investigated through field emission gun-scanning electron microscopy and transmission electron microscopy, which revealed that nano flowers of ZnO were deposited on the HAp surface. ZnO/Zn-doped HAps was impregnated with alizarin (AZ) at pH 4 and 8.5, resulting in hybrid pigments with varying hues of red. Attenuated total reflectance-Fourier transform infrared spectroscopy, UV-vis spectroscopy, and X-ray photoelectron spectroscopy suggested that better solids@dye interactions occurred at pH 8.5, and as indicated by C1s spectra, the appearance of the peak at 286.5 eV (C = O)

and an increase in the peak intensity at 284.6 eV (C--C/H) confirmed the adsorption of the dye on the surface. Photodegradation tests revealed that the prepared pigments were highly stable after exposure to light.

APPLIED SURFACE SCIENCE 593, 153412, 2022. DOI: 10.1016/j.apsusc.2022.153412

[P156-2022] "Generation of nonclassical states of light via truncation of mixed states"

Mattos, E. P.*; Vidiella-Barranco, A.*

A possible way of generating nonclassical states of light is via the truncation of a given state in the Fock basis. In recent work, we presented an alternative scheme for such quantum scissors [Phys. Rev. A 104, 033715 (2021)], employing a nondegenerate parametric amplifier, a beam splitter, and photodetectors. An advantage of this setup is that it does not require the generation of Fock states beforehand, as in previous proposals. Here we extend this treatment to mixed input states. We show the possibilities of generating truncated states with either a maximum Fock number N or states having a minimum Fock number N. We discuss two specific examples of states to be truncated: (i) the thermal state and (ii) the phase-diffused coherent state. In either case, the generated field states can present sub-Poissonian statistics as well as non-Gaussian character. These nonclassical properties can be adjusted by changing the parameters of the scissors, e.g., the amplifier strength and the beam-splitter transmittance.

JOURNAL OF THE OPTICAL SOCIETY OF AMERICA B-OPTICAL PHYSICS 39[7], 1885-1893, 2022. DOI: 10.1364/JOSAB.450622

[P157-2022] "Global exploration of phase behavior in frustrated Ising models using unsupervised learning techniques"

Elias, D. R. D. de*; Granato, E.*; Koning, M. de*

We apply a set of machine-learning (ML) techniques for the global exploration of the phase diagrams of two frustrated 2D Ising models with competing interactions. Based on raw Monte Carlo spin configurations generated for random system parameters, we apply principal-component analysis (PCA) and auto-encoders to achieve dimensionality reduction, followed by clustering using the DBSCAN method and a support--vector machine classifier to construct the transition lines between the distinct phases in both models. The results are in very good agreement with available exact solutions, with the auto-encoders leading to quantitatively superior estimates, even for a data set containing only 1400 spin configurations. In addition, the results suggest the existence of a relationship between the structure of the optimized auto--encoder latent space and physical characteristics of both systems. This indicates that the employed approach can be useful in perceiving fundamental properties of physical systems in situations where a priori theoretical insight is unavailable.

PHYSICA A-STATISTICAL MECHANICS AND ITS APPLICATIONS 589, 126653, 2022. DOI: 10.1016/j.physa.2021.126653

[P158-2022] "Guided fractures in graphene mechanical diode-like structures"

Felix, L. C.*; Galvao, D. S.*

The concept of a diode is usually applied to electronic and thermal devices but very rarely for mechanical ones. A recently proposed fracture rectification effect in polymer-based structures with triangular void defects has motivated us to test these ideas at the nanoscale using graphene membranes. Using fully-atomistic reactive molecular dynamics simulations we showed that robust rectification-like effects exist. The fracture can be 'guided' to more easily propagate along one specific direction than its opposite. We also observed that there is an optimal value for the spacing between each void for the rectification effect.

PHYSICAL CHEMISTRY CHEMICAL PHYSICS 24[22], 13905-13910, 2022. DOI: 10.1039/d2cp01207c

[P159-2022] "Heterophase Interface and Surface Functionalization of TiOx/TiSix Metastable Nanofilms"

Echeverrigaray, F. G.*; Figueroa, C. A.; Zanatta, A. R.; **Alvarez, F.***

In this paper, topographically asymmetric TiOx/TiSix metastable ultrathin (nano)films on SiO2/Si(100) are produced by controlling interface reactions through ion beam synthesis. The film growth process involves a dual ion beam system, combining Ar+ sputtering a Ti target and in situ postirradiation (Ar+ + H-2(+) ion etching) at normal incidence to modify the surface morphology. The film's production and characterization are challenging due to the formation of a complex mixed interface+layers (heterophases) containing nanocrystalline and amorphous compounds of Ti and Si. The results for different ion etching times (0-600 s) are systematically presented and analyzed. With the experimental+theoretical information, it is possible to deduce that the heterophase interface is originated by oxide intermixing in combination with the formation of titanium silicides taking place at the early stages of growth. The reactivity of oxygen and hydrogen species is the dominating factor influencing the metastable film growth mediated by solid-state phase reactions. Given its crucial role at the (Ti/Si):O interface, the chemical route and control of intrinsic defects (non-stoichiometry) are defined by domain ordering mechanisms followed by surface restructuring. In view of their main characteristics, taken altogether, the current functional metastable films represent a promising alternative for high-performance photonic and optoelectronic applications.

ADVANCED MATERIALS INTERFACES, 2200799, 2022. DOI: 10.1002/admi.202200799, **Primeira data de acesso:** JUL 2022

[P160-2022] "Humins-Like Solid Support for Palladium Immobilization: Highly Efficient and Recyclable Catalyst for Cross-Coupling Reactions"

Galaverna, R. S.; Fernandes, L. P.; Silva, V. H. M. da; **Siervo, A. de***; Pastre, J. C.

In the present work, a new humins-like resin was prepared using 2,5-bis(hydroxymethyl)furan (DHMF) and maleic anhydride in 2 min at 110 degrees C. Such a new material was used as a solid support for palladium immobilization. For metal anchoring, encapsulation was the method of choice and palladium was encapsulated by in-situ polymerization. This resulting Pd@DHMF-based catalyst was characterized by solid-state C-13 NMR, FT-IR, SEM, TGA, DSC, XRD, and XPS. To demonstrate proof of concept, Heck and Suzuki cross-coupling reactions were selected to evaluate the activity and reusability of the catalyst. Green solvents such as gamma-valerolactone (GVL), Cyrene (TM) and ethylene carbonate proved to be excellent reaction media for Heck coupling, whereas EtOH/H2O was preferred for Suzuki coupling. Yields of up to 99 % were obtained in both cases. The recyclability of the Pd@DHMF-based catalyst was also demonstrated, 7 cycles have been achieved without loss of catalytic activity in both Heck and Suzuki reactions.

EUROPEAN JOURNAL OF ORGANIC CHEMISTRY 2022[24], e202200376, 2022. DOI: 10.1002/ejoc.202200376

[P161-2022] "Hypertriton Production in p-Pb Collisions at root S-NN =5.02 TeV"

Acharya, S.; Adamova, D.; **Chinellato, D. D.*; Guardiano, G. G.*; Jahnke, C.*; Takahashi, J.***; et al. Large Ion Collider Expt Collaborat

The study of nuclei and antinuclei production has proven to be a powerful tool to investigate the formation mechanism of loosely bound states in high-energy hadronic collisions. The first measurement of the production of H-3(Lambda) in p-Pb collisions at root S-NN = 5.02 TeV is presented in this Letter. Its production yield measured in the rapidity interval -1 < y <0 for the 40% highest-multiplicity p-Pb collisions is dN/dy = [6.3 +/- 1.8(stat) +/- 1.2(syst)] x 10(-7). The measurement is compared with the expectations of statistical hadronization and coalescence models, which describe the nucleosynthesis in hadronic collisions. These two models predict very different yields of the hypertriton in charged particle multiplicity environments relevant to small collision systems such as p-Pb, and therefore the measurement of dN/dy is crucial to distinguish between them. The precision of this measurement leads to the exclusion with a significance larger than 6.9 sigma of some configurations of the statistical hadronization model, thus constraining the theory behind the production of loosely bound states at hadron colliders.

PHYSICAL REVIEW LETTERS 128[25], 252003, 2022. DOI: 10.1103/PhysRevLett.128.252003

[P162-2022] "Inclusive, prompt and non-prompt J/psi production at midrapidity in p-Pb collisions at root s(NN)=5.02 TeV"

Acharya, S.; Adamova, D.; **Chinellato, D. D.*; Guardiano, G. G.*; Jahnke, C.*; Takahashi, J.***; et al. ALICE Collaboration

A measurement of inclusive, prompt, and non-prompt J/psi production in p-Pb collisions at a nucleon-nucleon centre-of--mass energy root s(NN) = 5.02 TeV is presented. The inclusive J/psi mesons are reconstructed in the dielectron decay channel at midrapidity down to a transverse momentum p(T) = 0. The inclusive J/psi nuclear modification factor R-pPb is calculated by comparing the new results in p-Pb collisions to a recently measured proton-proton reference at the same centre-of-mass energy. Non-prompt J/psi mesons, which originate from the decay of beauty hadrons, are separated from promptly produced J/psi on a statistical basis for p(T) larger than 1.0 GeV/c. These results are based on the data sample collected by the ALICE detector during the 2016 LHC p-Pb run, corresponding to an integrated luminosity L-int = 292 +/- 11 mu b(-1), which is six times larger than the previous publications. The total uncertainty on the P-T-integrated inclusive J/psi and non-prompt J/psi cross section are reduced by a factor 1.7 and 2.2, respectively. The measured cross sections and R-pPb are compared with theoretical models that include various combinations of cold nuclear matter effects. From the non-prompt J/psi production cross section, the b (b) over bar production cross section at midrapidity, d sigma(b (b) over bar)/dy, and the total cross section extrapolated over full phase space sigma(b (b) over bar) are derived.

JOURNAL OF HIGH ENERGY PHYSICS [6], 011, 2022. DOI: 10.1007/JHEP06(2022)011

[P163-2022] "Investigating the role of strangeness in baryon-antibaryon annihilation at the LHC"

Acharya, S.; Adamova, D.; **Chinellato, D. D.*; Guardiano, G. G.*; Jahnke, C.*; Takahashi, J.***; et al. ALICE Collaboration

Annihilation dynamics plays a fundamental role in the baryon-antibaryon interaction (B-(B) over bar) at low--energy and its strength and range are crucial in the assessment of possible baryonic bound states. Experimental data on annihilation cross sections are available for the p-(p) over bar system but not in the low relative momentum region. Data regarding the B-(B) over bar interaction with strange degrees of freedom are extremely scarce, hence the modeling of the annihilation contributions is mainly based on nucleon-antinucleon (N-(N) over bar) results, when available. In this letter we present a measurement of the p-(p) over bar, p-(Lambda) over bar circle plus(p) over bar-Lambda and Lambda-(Lambda) over bar interaction using correlation functions in the relative momentum space in high-multiplicity triggered pp collisions at root s = 13 TeV recorded by ALICE at the LHC. In the p-(p) over bar system the couplings to the mesonic channels in different partial waves are extracted by adopting a coupled-channel approach with recent chi EFT potentials. The inclusion of these inelastic channels provides good agreement with the data, showing a significant presence of the annihilation term down to zero momentum. Predictions obtained using the Lednicky-Lyuboshits formula and scattering parameters obtained from heavy-ion collisions, hence mainly sensitive to elastic processes, are compared with the experimental p-(Lambda) over bar circle plus(p) over bar-Lambda and Lambda-(Lambda) over bar correlations. The model describes the Lambda-(Lambda) over bar data and underestimates the p-(Lambda) over bar circle plus(p) over bar-Lambda data in the region of momenta below 200 MeV/c. The observed deviation indicates a different contribution of annihilation channels to the two systems containing strange hadrons.

PHYSICS LETTERS B 829, 137060, 2022. DOI: 10.1016/j.physletb.2022.137060

[P164-2022] "Kibble-Zurek Scaling from Linear Response Theory"

Naze, P.*; Bonanca, M. V. S.*; Deffner, S.*

While quantum phase transitions share many characteristics with thermodynamic phase transitions, they are also markedly different as they occur at zero temperature. Hence, it is not immediately clear whether tools and frameworks that capture the properties of thermodynamic phase transitions also apply in the quantum case. Concerning the crossing of thermodynamic critical points and describing its non-equilibrium dynamics, the Kibble-Zurek mechanism and linear response theory have been demonstrated to be among the very successful approaches. In the present work, we show that these two approaches are also consistent in the description of quantum phase transitions, and that linear response theory can even inform arguments of the Kibble-Zurek mechanism. In particular, we show that the relaxation time provided by linear response theory gives a rigorous argument for why to identify the "gap" as a relaxation rate, and we verify that the excess work computed from linear response theory exhibits Kibble-Zurek scaling.

ENTROPY 24[5], 666, 2022. DOI: 10.3390/e24050666

[P165-2022] "Low exposure long-baseline neutrino oscillation sensitivity of the DUNE experiment"

Abud, A. A.; Abi, B.; Acciarri, R.; **Belchior, E.*; Holanda, P. C. de*; Souza, G. de*; Gelli, B.*; Giammaria, P.*; Guzzo, M. M.*; Kemp, E.*; Machado, A. A.*; Peres, O. L. G.*; Prakash, S.*; Segreto, E.*; Souza, H. V. de***; et al. DUNE Collaboration

The Deep Underground Neutrino Experiment (DUNE) will produce world-leading neutrino oscillation measurements over the lifetime of the experiment. In this work, we explore DUNE's sensitivity to observe charge-parity violation (CPV) in the neutrino sector, and to resolve the mass ordering, for exposures of up to 100 kiloton-megawatt-calendar years (kt-MW-CY), where calendar years include an assumption of 57% accelerator uptime based on past accelerator performance at Fermilab.

The analysis includes detailed uncertainties on the flux prediction, the neutrino interaction model, and detector effects. We demonstrate that DUNE will be able to unambiguously resolve the neutrino mass ordering at a 4 sigma (5 sigma) level with a 66 (100) kt-MW-CY far detector exposure, and has the ability to make strong statements at significantly shorter exposures depending on the true value of other oscillation parameters, with a median sensitivity of 3 sigma for almost all true delta(CP) values after only 24 kt-MW-CY. We also show that DUNE has the potential to make a robust measurement of CPV at a 3 sigma level with a 100 kt-MW-CY exposure for the maximally CP-violating values delta(CP) = +/-pi/2. Additionally, the dependence of DUNE's sensitivity on the exposure taken in neutrino-enhanced and antineutrino-enhanced running is discussed. An equal fraction of exposure taken in each beam mode is found to be close to optimal when considered over the entire space of interest.

PHYSICAL REVIEW D 105[7], 072006, 2022. DOI: 10.1103/PhysRevD.105.072006

[P166-2022] "Measurement of K*(892)(+/-) production in inelastic pp collisions at the LHC"

Acharya, S.; Adamova, D.; **Chinellato, D. D.*; Guardiano, G. G.*; Jahnke, C.*; Takahashi, J.***; et al. ALICE Collaboration

The first results on K*(892)(+/-) resonance production in inelastic pp collisions at LHC energies of root s = 5.02, 8, and 13 TeV are presented. The K*(892)(+/-) (;)has been reconstructed via its hadronic decay channel K*(892)(+/-) -> K-S(0) + pi(+/-) with the ALICE detector. Measurements of transverse momentum distributions, p(T)-integrated yields, and mean transverse momenta for charged K*(892) are found to be consistent with previous ALICE measurements for neutral K*(892) within uncertainties. For p(T) > 1 GeV/c the K*(892)(+/-) transverse momentum spectra become harder with increasing centre-of-mass energy from 5.02 to 13 TeV, similar to what previously observed for charged kaons and pions. For p(T) < 1 GeV/c the K*(892)(+/-) yield does not evolve significantly and the abundance of K*(892)(+/-) relative to K is rather independent of the collision energy. The transverse momentum spectra, measured for K*(892)(+/-) at midrapidity in the interval 0 < p(T) < 15 GeV/c, are not well described by predictions of different versions of PYTHIA 6, PYTHIA 8 and EPOS-LHC event generators. These generators reproduce the measured p(T)-integrated K*(+/-)/K ratios and describe well the momentum dependence for p(T) < 2 GeV/c.

PHYSICS LETTERS B 828, 137013, 2022. DOI: 10.1016/j.physletb.2022.137013

[P167-2022] "Measurement of prompt D-s(+)-meson production and azimuthal anisotropy in Pb-Pb collisions at root s(NN)=5.02 TeV"

Acharya, S.; Adamova, D.; **Chinellato, D. D.*; Guardiano, G. G.*; Jahnke, C.*; Takahashi, J.***; et al. ALICE Collaboration

The production yield and angular anisotropy of prompt D-s(+) mesons were measured as a function of transverse momentum (p(T)) in Pb-Pb collisions at a centre-of-mass energy per nucleon pair root s(NN) = 5.02 TeV collected with the ALICE detector at the LHC. D-s(+) mesons and their charge conjugates were reconstructed at midrapidity (vertical bar y vertical bar < 0.5) from their hadronic decay channel D-s(+) -> phi pi(+), with phi -> K-K+, in the p(T) intervals 2 < p(T) < 50 GeV/c and 2 < p(T) < 36 GeV/c for the 0-10% and 30-50% centrality intervals. For p(T) > 10 GeV/c, the measured D-s(+)-meson nuclear modification factor R-AA is consistent with the one of non-strange D mesons within uncertainties, while at lower p(T) a hint for a D-s(+)--meson R-AA larger than that of non-strange D mesons is seen. The enhanced production of D-s(+) relative to non-strange D mesons is also studied by comparing the p(T)-dependent D--s(+)/D-0 production yield ratios in Pb-Pb and in pp collisions. The ratio measured in Pb-Pb collisions is found to be on average higher than that in pp collisions in the interval 2 < p(T) < 8 GeV/c with a significance of 2.3 sigma and 2.4 sigma for the 0-10% and 30-50% centrality intervals. The azimuthal anisotropy coefficient v(2) of prompt D-s(+) mesons was measured in Pb-Pb collisions in the 30-50% centrality interval and is found to be compatible with that of non-strange D mesons. The main features of the measured R-AA, D-s(+)/D-0 ratio, and v(2) as a function of p(T) are described by theoretical calculations of charm--quark transport in a hydrodynamically expanding quark-gluon plasma including hadronisation via charm-quark recombination with light quarks from the medium. The p(T)-integrated production yield of D-s(+) mesons is compatible with the prediction of the statistical hadronisation model.

PHYSICS LETTERS B 827, 136986, 2022. DOI: 10.1016/j.physletb.2022.136986

[P168-2022] "Measurement of the inclusive and differential WZ production cross sections, polarization angles, and triple gauge couplings in pp collisions at root s=13 TeV"

Tumasyan, A.; Adam, W.; **Chinellato, J. A.***; et al. CMS Collaboration

The associated production of a W and a Z boson is studied in final states with multiple leptons produced in proton-proton (pp) collisions at a centre-of-mass energy of 13 TeV using 137 fb(-1) of data collected with the CMS detector at the LHC. A measurement of the total inclusive production cross section yields sigma(tot)(pp -> WZ) = 50.6 +/- 0.8 (stat) +/- 1.5 (syst) +/- 1.1 (lumi) +/- 0.5 (theo) pb. Measurements of the fiducial and differential cross sections for several key observables are also performed in all the final-state lepton flavour and charge compositions with a total of three charged leptons, which can be electrons or muons. All results are compared with theoretical predictions computed up to next-to-next-to-leading order in quantum chromodynamics plus next-to-leading order in electroweak theory and for various sets of parton distribution functions. The results include direct measurements of the charge asymmetry and the W and Z vector boson polarization. The first observation of longitudinally polarized W bosons in WZ production is reported. Anomalous gauge couplings are searched for, leading to new constraints on beyond-the--standard-model contributions to the WZ triple gauge coupling.

JOURNAL OF HIGH ENERGY PHYSICS [7], 032, 2022. DOI: 10.1007/JHEP07(2022)032

[P169-2022] "Measurement of the production cross section for Z plus b jets in proton-proton collisions at root s=13 TeV"

Tumasyan, A.; Adam, W.; **Chinellato, J. A.***; et al. CMS Collaboration

The measurement of the cross section for the production of a Z boson, decaying to dielectrons or dimuons, in association with at least one bottom quark jet is performed with proton--proton collision data at ffiffi s p ¼ 13 TeV. The data sample corresponds to an integrated luminosity of 137 fb−1, collected by the CMS experiment at the LHC during 2016–2018. The integrated cross sections for Zþ ≥ 1 b jet and Zþ ≥ 2 b jets are reported for the electron, muon, and combined channels. The fiducial cross sections in the combined channel are 6.52 0.04ðstatÞ 0.40ðsystÞ 0.14ðtheoÞ pb for Zþ ≥ 1 b jet and 0.65 0.03ðstatÞ 0.07ðsystÞ 0.02ðtheoÞ pb for Zþ ≥ 2 b jets.

The differential cross section distributions are measured as functions of various kinematic observables that are useful for precision tests of perturbative quantum chromodynamics predictions. The ratios of integrated and differential cross sections for Zþ ≥ 2b jets and Zþ ≥ 1 b jet processes are also determined. The value of the integrated cross section ratio measured in the combined channel is 0.100 0.005ðstatÞ 0.007ðsystÞ 0.003ðtheoÞ. All measurements are compared with predictions from various event generators.

PHYSICAL REVIEW D 105[9], 092014, 2022. DOI: 10.1103/PhysRevD.105.092014

[P170-2022] "Multiplicity dependence of charged-particle jet production in pp collisions at root s=13 TeV"

Acharya, S.; Adamova, D.; **Chinellato, D. D.*; Guardiano, G. G.*; Jahnke, C.*; Takahashi, J.***; et al. ALICE Collaboration

The multiplicity dependence of jet production in pp collisions at the centre-of-mass energy of root s = 13 TeV is studied for the first time. Jets are reconstructed from charged particles using the anti-k(T) algorithm with resolution parameters R varying from 0.2 to 0.7. The jets are measured in the pseudorapidity range vertical bar eta(jet)vertical bar < 0.9 - R and in the transverse momentum range 5 < P-T,jet(ch) < 140 GeV/c. The multiplicity intervals are categorised by the ALICE forward detector V0. The p(T)differential cross section of charged-particle jets are compared to leading order (LO) and next-to-leading order (NLO) perturbative quantum chromodynamics (pQCD) calculations. It is found that the data are better described by the NLO calculation, although the NLO prediction overestimates the jet cross section below 20 GeV/c. The cross section ratios for different R are also measured and compared to model calculations. These measurements provide insights into the angular dependence of jet fragmentation. The jet yield increases with increasing self-normalised charged-particle multiplicity. This increase shows only a weak dependence on jet transverse momentum and resolution parameter at the highest multiplicity. While such behaviour is qualitatively described by the present version of PYTHIA, quantitative description may require implementing new mechanisms for multi-particle production in hadronic collisions.

EUROPEAN PHYSICAL JOURNAL C 82[6], 514, 2022. DOI: 10.1140/epjc/s10052-022-10405-z

[P171-2022] "Neutrinos in a Minimal 3-3-1 Model"

Guzzo, M. M.*; Leite, L. J. F.*; Novelo, S. W. P.*

In this work, we present a general review of neutrino physics in the minimal 331 model. New gauge and scalar interactions are present, with violation of both flavor and lepton numbers. Including mixing angles and possible CP-violating phases, 15 new parameters arise in vector and scalar neutrino interactions. We also bring to light a discussion at the different neutrino bases that naturally appear in most beyond the Standard Model physics and, in particular, in the minimal 331 model.

FRONTIERS IN PHYSICS 10, 812921, 2022. DOI: 10.3389/fphy.2022.812921

[P172-2022] "Nuclear modification factor of light neutral--meson spectra up to high transverse momentum in p-Pb collisions at root S-NN=8.16 TeV"

Acharya, S.; Adamova, D.; **Chinellato, D. D.*; Guardiano, G. G.*; Jahnke, C.*; Takahashi, J.***; et al. ALICE Collaboration

Neutral pion(pi(0)) and eta meson production cross sections were measured up to unprecedentedly high transverse momenta (p(T)) in p-Pb collisions at root s(NN) = 8.16 TeV. The mesons were reconstructed via their two-photon decay channel in the rapidity interval -1.3 < y < 0.3 in the ranges of 0.4 < p(T) < 200 GeV/cand 1.0 < p(T) < 50 GeV/c, respectively. The respective nuclear modification factor (R-pPb) is presented for p(T) up to of 200 and 30 GeV/c, where the former was achieved by extending the pi(0) measurement in pp collisions at root s = 8 TeV using the merged cluster technique. The values of R-pPb are below unity for p(T) < 10 GeV/c, while they are consistent with unity for p(T) > 10 GeV/c, leaving essentially no room for final state energy loss. The new data provide strong constraints for nuclear parton distribution and fragmentation functions over a broad kinematic range and are compared to model predictions as well as previous results at root s(NN) = 5.02 TeV. Funded by SCOAP(3).

PHYSICS LETTERS B 827, 136943, 2022. DOI: 10.1016/j.physletb.2022.136943

[P173-2022] "Observation of a multiplicity dependence in the p(T)-differential charm baryon-to-meson ratios in proton-proton collisions at root s=13 TeV"

Acharya, S.; Adamova, D.; **Chinellato, D. D.*; Guardiano, G. G.*; Jahnke, C.*; Takahashi, J.***; et al. ALICE Collaboration

The production of prompt D-0, D-s(+) and Lambda(+)(c) hadrons, and their ratios, D-s(+)/D-0 and Lambda(+)(c)/D-0, are measured in proton-proton collisions at root s = 13 TeV at midrapidity (vertical bar y vertical bar < 0.5) with the ALICE detector at the LHC. The measurements are performed as a function of the charm-hadron transverse momentum (p(T)) in intervals of charged-particle multiplicity, measured with two multiplicity estimators covering different pseudorapidity regions. While the strange to non-strange D-s(+)/D-0 ratio indicates no significant multiplicity dependence, the baryon-to-meson P-T-differential Lambda(+)(c)/D-0 ratio shows a multiplicity-dependent enhancement, with a significance of 5.3 sigma for 1 < p(T) < 12 GeV/c, comparing the highest multiplicity interval with respect to the lowest one. The measurements are compared with a theoretical model that explains the multiplicity dependence by a canonical treatment of quantum charges in the statistical hadronisation approach, and with predictions from event generators that implement colour reconnection mechanisms beyond the leading colour approximation to model the hadronisation process. The Lambda(+)(c)/D-0 ratios as a function of p(T) present a similar shape and magnitude as the Lambda/K-s(0) ratios in comparable multiplicity intervals, suggesting a potential common mechanism for light- and charmhadron formation, with analogous multiplicity dependence. The p(T)-integrated ratios, extrapolated down to p(T) = 0, do not show a significant dependence on multiplicity within the uncertainties.

PHYSICS LETTERS B 829, 137065, 2022. DOI: 10.1016/j.physletb.2022.137065

[P174-2022] "Observation of B-s(0) mesons and measurement of the B-s(0)/B+ yield ratio in PbPb collisions at root S-NN=5.02 TeV"

Tumasyan, A.; Adam, W.; **Chinellato, J. A.*; Tonelli Manganote, E. J.***; et al. CMS Collaboration

The B-s(0) and B+ production yields are measured in PbPb collisions at a center-of-mass energy per nucleon pair of 5.02 TeV. The data sample, collected with the CMS detector at the LHC, corresponds to an integrated luminosity of 1.7 nb(-1).

The mesons are reconstructed in the exclusive decay channels B-s(0) -> J/psi (mu(+)mu(-))phi(K+K-) and B+ -> J/psi(mu(+)mu(-)) K+ in the transverse momentum range 7-50 GeV/c and absolute rapidity 0-2.4. The B-s(0) meson is observed with a statistical significance in excess of five standard deviations for the first time in nucleus-nucleus collisions. The measurements are performed as functions of the transverse momentum of the B mesons and of the PbPb collision centrality. The ratio of production yields of B-s(0) and B+ is measured and compared to theoretical models that include quark recombination effects.

PHYSICS LETTERS B 829, 137062, 2022. DOI: 10.1016/j.physletb.2022.137062

[P175-2022] "Observation of the B-c(+) Meson in Pb-Pb and pp Collisions at root s(NN)=5.02 TeV and Measurement of its Nuclear Modification Factor"

Tumasyan, A.; Adam, W.; **Chinellato, J. A.***; et al. CMS Collaboration

The B-c(+) meson is observed for the first time in heavy ion collisions. Data from the CMS detector are used to study the production of the B-c(+) meson in lead-lead (Pb-Pb) and proton-proton (pp) collisions at a center of-mass energy per nucleon pair of root s(NN) = 5.02 TeV, via the B-c(+) -> (J/psi -> mu(+)mu(-))mu(+)nu(mu) decay. The B-c(+) nuclear modification factor, derived from the Pb-Pb-to-pp ratio of production cross sections, is measured in two bins of the trimuon transverse momentum and of the Pb-Pb collision centrality. The B-c(+) meson is shown to be less suppressed than quarkonia and most of the open heavy-flavor mesons, suggesting that effects of the hot and dense nuclear matter created in heavy ion collisions contribute to its production. This measurement sets forth a promising new probe of the interplay of suppression and enhancement mechanisms in the production of heavy-flavor mesons in the quark-gluon plasma.

PHYSICAL REVIEW LETTERS 128[25], 252301, 2022. DOI: 10.1103/PhysRevLett.128.252301

[P176-2022] "Out-of-plane thermoelectric performance for p-doped GeSe"

Chaves, A. S.*; Larson, D. T.; Kaxiras, E.; **Antonelli, A.***

The record-breaking thermoelectric performance of tin selenide (SnSe) has motivated the investigation of analog compounds with the same structure. A promising candidate that emerged recently is germanium selenide (GeSe). Here, using extensive first-principles calculations of the hole-phonon and hole-impurity scattering, we investigate the thermoelectric transport properties of the orthorhombic phase of p--doped GeSe. We predict outstanding thermoelectric performance for GeSe over a broad range of temperatures due to its high Seebeck coefficients, extremely low Lorenz numbers, ultralow total thermal conductivity, and relatively large band gap. In particular, the out-of-plane direction in GeSe presents equivalent or even higher performance than SnSe for temperatures above 500 K. By extending the analysis to 900 K, we obtained an ultrahigh value for the thermoelectric figure of merit (zT = 3.2) at the optimal hole density of 4 x 10(19) cm(3). Our work provides strong motivation for continued experimental work focusing on improving the GeSe doping efficiency in order to achieve this optimal hole density.

PHYSICAL REVIEW B 105[20], 205201, 2022. DOI: 10.1103/PhysRevB.105.205201

[P177-2022] "Photophysical and Photoelectrochemical Properties of CsPbBr3 Films Grown by Electrochemically Assisted Deposition"

Gau, D. L.; Ramirez, D.; **Iikawa, F.***; Riveros, G.; Diaz, P.; Verdugo, J.; Nunez, G.; Lizama, S.; Lazo, P.; Dalchiele, E. A.; Contreras, L.; Idigoras, J.; Anta, J.; Marotti, R. E.

Perovskite have had a great impact on the solid-state physics world in the last decade not only achieving great success in photovoltaics but, more recently, also in the implementation of other optoelectronic devices. One of the main obstacles for the adoption of Pb-based perovskite technologies are the high amounts of Pb needed in the conventional preparation methods. Here we present for the first time a detailed analysis of the photophysical and photoelectrochemical properties of CsPbBr3 films directly grown on fluorine-doped tin oxide (FTO) coated glass through a novel technique based in the electrodeposition of PbO2 as CsPbBr3 precursor. This technique allows to save up to 90 % of the Pb used compared to traditional methods and can be scalable compared with the commonly used spin-coating process. The low temperature analysis of their photoluminescence spectra, performed in both steady state and time dependence, revealed a strong interaction between electrons and longitudinal optical (LO) phonons dominant at high temperatures. On the other hand, the electrochemical and photoelectrochemical analysis proves that CsPbBr3 prepared using this new method has state-of--the-art features, showing a p-type behavior under depletion regime. This is also confirmed by photoelectrochemical measurements using p-benzoquinone as target molecule. These results prove that the proposed method can be used to produce excellent CsPbBr3 films, saving much of the lead waste.

CHEMPHYSCHEM e202200286, 2022. DOI: 10.1002/cphc.202200286

[P178-2022] "Polarization of Lambda and (Lambda)over-bar Hyperons along the Beam Direction in Pb-Pb Collisions at root s(NN)=5.02 TeV"

Acharya, S.; Adamova, D.; **Chinellato, D. D.*; Guardiano, G. G.*; Jahnke, C.*; Takahashi, J.***; et al. ALICE Collaboration

The polarization of the Lambda and (Lambda) over bar hyperons along the beam (z) direction, P-z, has been measured in Pb-Pb collisions at root s(NN) = 5.02 TeV recorded with ALICE at the Large Hadron Collider (LHC). The main contribution to P-z comes from elliptic flow-induced vorticity and can be characterized by the second Fourier sine coefficient P-z,P-s2 = < P-z sin(2 phi - 2 Psi(2))>, where phi is the hyperon azimuthal emission angle and Psi(2) is the elliptic flow plane angle. We report the measurement of P-z,P-s2 for different collision centralities and in the 30%-50% centrality interval as a function of the hyperon transverse momentum and rapidity. The P-z,P-s2 is positive similarly as measured by the STAR Collaboration in Au--Au collisions at root s(NN) = 200 GeV, with somewhat smaller amplitude in the semicentral collisions. This is the first experimental evidence of a nonzero hyperon P-z in Pb-Pb collisions at the LHC. The comparison of the measured P-z,P-s2 with the hydrodynamic model calculations shows sensitivity to the competing contributions from thermal and the recently found shear-induced vorticity, as well as to whether the polarization is acquired at the quark-gluon plasma or the hadronic phase.

PHYSICAL REVIEW LETTERS 128[17], 172005, 2022. DOI: 10.1103/PhysRevLett.128.172005

[P179-2022] "Precision measurement of the W boson decay branching fractions in proton-proton collisions at root s=13 TeV"

Tumasyan, A.; Adam, W.; **Chinellato, J. A.***; et al. CMS Collaboration

The leptonic and inclusive hadronic decay branching fractions of the W boson are measured using proton-proton collision data collected at p s = 13 TeV by the CMS experiment at the CERN LHC, corresponding to an integrated luminosity of 35.9 fb???1. Events characterized by the production of one or two W bosons are selected and categorized based on the multiplicity and flavor of reconstructed leptons, the number of jets, and the number of jets identified as originating from the hadronization of b quarks. A binned maximum likelihood estimate of the W boson branching fractions is performed simultaneously in each event category. The measured branching fractions of the W boson decaying into electron, muon, and tau lepton final states are (10.83 ?? 0.10)%, (10.94 ?? 0.08)%, and (10.77 ?? 0.21)%, respectively, consistent with lepton flavor universality for the weak interaction. The average leptonic and inclusive hadronic decay branching fractions are estimated to be (10.89 ?? 0.08)% and (67.32 ?? 0.23)%, respectively. Based on the hadronic branching fraction, three standard model quantities are subsequently derived: the sum of squared elements in the first two rows of the Cabibbo???Kobayashi???Maskawa (CKM) matrix Pij IVijI2 = 1.984 ?? 0.021, the CKM element IVcsI = 0.967 ?? 0.011, and the strong coupling constant at the W boson mass scale, ??S(m2W) = 0.095 ?? 0.033.

PHYSICAL REVIEW D 105[7], 072008, 2022. DOI: 10.1103/PhysRevD.105.072008

[P180-2022] "Probing Charm Quark Dynamics via Multiparticle Correlations in Pb-Pb Collisions at root s(NN)=5.02 TeV"

Tumasyan, A.; Adam, W.; **Chinellato, J. A.***; et al. CMS Collaboration; CMS Collaboration

Multiparticle azimuthal correlations of prompt D-0 mesons arc measured in Pb-Pb collisions at a nucleon-nucleon center-of--mass energy of root s(NN) = 5.02 TeV. For the first time, a four-particle cumulant method is used to extract the second Fourier coefficient of the azimuthal distribution (v(2)) of D-0 mesons as a function of event centrality and the D-0 transverse momentum. The ratios of the four-particle v(2) values to previously measured two-particle cumulant results provide direct experimental access to event-by-event fluctuations of charm quark azimuthal anisotropies. These ratios are also found to be comparable to those of inclusive charged particles in the event. However, hints of deviations are seen in the most central and peripheral collisions. To investigate the origin of flow fluctuations in the charm sector, these measurements are compared to a model implementing fluctuations of charm quark energy loss via collisional or radiative processes in the quark-gluon plasma. These models cannot quantitatively describe the data over the full transverse momentum and centrality ranges, although the calculations with collisional energy loss provide a better description of the data.

PHYSICAL REVIEW LETTERS 129[2], 022001, 2022. DOI: 10.1103/PhysRevLett.129.022001

[P181-2022] "Production of Lambda and K-S(0) in jets in p-Pb collisions at root s(NN)=5.02 TeV and pp collisions at root s=7 TeV"

Acharya, S.; Adamova, D.; **Chinellato, D. D.*; Guardiano, G. G.*; Jahnke, C.*; Takahashi, J.*;** et al. ALICE Collaboration

The production of A baryons and K-S(0) mesons (V-0 particles) was measured in p-Pb collisions at root s(NN) = 5.02 TeV and pp collisions at root s = 7 TeV with ALICE at the LHC. The production of these strange particles is studied separately for particles associated with hard scatterings and the underlying event to shed light on the baryon-to-meson ratio enhancement observed at intermediate transverse momentum (p(T)) in high multiplicity pp and p-Pb collisions. Hard scatterings are selected on an event by-event basis with jets reconstructed with the anti-k(T) algorithm using charged particles. The production of strange particles associated with jets p(T,jet)(ch) > 10 and p(T,jet)(ch) > 20 GeV/c in p-Pb collisions, and with jet p(T,jet)(ch) > 10 GeV/c in pp collisions is reported as a function of p(T). Its dependence on angular distance from the jet axis, R(V-0, jet), for jets with p(T,jet)(ch) > 10 GeV/c in p-Pb collisions is reported as well. The p(T)-differential production spectra of strange particles associated with jets are found to be harder compared to that in the underlying event and both differ from the inclusive measurements. In events containing a jet, the density of the V-0 particles in the underlying event is found to be larger than the density in the minimum bias events. The Lambda/K-S(0) ratio associated with jets in p-Pb collisions is consistent with the ratio in pp collisions and follows the expectation of jets fragmenting in vacuum. On the other hand, this ratio within jets is consistently lower than the one obtained in the underlying event and it does not show the characteristic enhancement of baryons at intermediate p(T) often referred to as "baryon anomaly" in the inclusive measurements. (c) 2022 European Organization for Nuclear Research, ALICE. Published by Elsevier B.V. Funded by SCOAP(3).

PHYSICS LETTERS B 827, 136984, 2022. DOI: 10.1016/j.physletb.2022.136984

[P182-2022] "RDM: An R interface for high-throughput simulation of ion-material interactions using TRIM"

Prearo, I.*; Lixandrao Filho, A. L.*; Guedes, S.*

The quantitative estimation of the damage caused by ion-material interaction is carried out using Monte Carlo codes as, for instance, TRIM (TRansport of Ions in Matter). Some studies require multiple simulations to be run, varying the ion energy, mass, and charge, or changing the target material. Natural radiation damage in minerals due to the alpha decays in the three natural series is an example. In such applications, the task of calculating the ion damage on the material becomes very time-consuming. The R language code presented in this paper, Radiation Damage in Materials (RDM), is designed to serve as an interface to set parameters, start, collect, and treat the results of multiple TRIM simulations. The main outputs of RDM are the dpa (displacements per atom) and dpa profiles for ion beam irradiation, and, if needed, the natural radiation dpa for any materials to be used in a given study. The fluence of an artificially accelerated ion beam matching the natural radiation dpa is also calculated for studies in which swift heavy ions are used as proxies for natural radiation damage.

COMPUTER PHYSICS COMMUNICATIONS 279, 108451, 2022. DOI: 10.1016/j.cpc.2022.108451

[P183-2022] "Redundantly Amplified Information Suppresses Quantum Correlations in Many-Body Systems"

Girolami, D.; Touil, A.; Yan, B.; **Deffner, S.*;** Zurek, W. H.

We establish bounds on quantum correlations in many-body systems. They reveal what sort of information about a quantum system can be simultaneously recorded in different parts of its environment. Specifically, independent agents who monitor environment fragments can eavesdrop only on amplified and redundantly disseminated—hence, effectively classical—information about the decoherence-resistant pointer observable.

We also show that the emergence of classical objectivity is signaled by a distinctive scaling of the conditional mutual information, bypassing hard numerical optimizations. Our results validate the core idea of quantum Darwinism: objective classical reality does not need to be postulated and is not accidental, but rather a compelling emergent feature of quantum theory that otherwise—in the absence of decoherence and amplification—leads to "quantum weirdness." In particular, a lack of consensus between agents that access environment fragments is bounded by the information deficit, a measure of the incompleteness of the information about the system.

PHYSICAL REVIEW LETTERS 129[1], 010401, 2022. DOI: 10.1103/PhysRevLett.129.010401

[P184-2022] "Resolving magnetic contributions in BiFeO3 nanoparticles using First order reversal curves"

Cardona-Rodriguez, A.; Rodriguez, E. R.; Carranza-Celis, D.; Vergara-Duran, N.; **Cruz, A. S. E. da*;** Londono, O. M.; **Knobel, M.*;** Reiber, A.; **Muraca, D.*;** Ramirez, J. G.

BiFeO3 (BFO) nanoparticles (NPs) were studied using First--Order Reversal Curve (FORC) and temperaturedependent magnetometry measurements. The BFO NPs were fabricated by a sol-gel method, while the crystal structure and the average particle radius were obtained by powder X-ray diffraction analysis and Small-Angle XRay Scattering (SAXS) measurements, respectively. The NP size varies below and above the typical bulk BFO spin cycloid length (lambda = 62 nm). Below lambda, the NPs show ferromagnetic-like hysteresis loops where the saturation magnetization decreases while nanoparticle size rises. This magnetic behavior changes for NP size over lambda, which only exhibits a paramagnetic contribution. The FORC distributions indicate the presence of two competing sizedependent contributions to the observed magnetic signal Also, the FORC distributions show that in the ferromagnetic regime there are two competing size-dependent contributions to the observed magnetic signal. Our results suggest the existence of a magnetic core-shell structure in NPs below lambda, possibly driven by the strong spin-lattice coupling.

JOURNAL OF MAGNETISM AND MAGNETIC MATERIALS 556, 169409, 2022. DOI: 10.1016/j.jmmm.2022.169409

[P185-2022] "Resorcinol-based carbon xerogel/ZnO composite for solar-light-induced photodegradation of sulfamerazine"

Moraes, N. P. de; Rocha, R. D. da S.; **Siervo, A. de*;** Prado, C. C. A. do; Paiva, T. C. B. de; Campos, T. M. B.; Thim, G. P.; Lanza, M. R. D. V.; Rodrigues, L. A.

Recently, the release of antibiotics, such as sulfonamides, into the environment has raised significant concern due to the potential creation of antibiotic-resistant bacteria. Thus, the development of remediation technologies for effluents containing such compounds is of utmost urgency. In this context, this work evaluated the creation of a resorcinol-based carbon xerogel/zinc oxide photocatalyst (XC/ZnO) to efficiently promote the photodegradation of the antibiotic known as sulfamerazine in aqueous media. The employment of this carbonaceous structure as a co-catalyst is justified by its high surface area and electrical conductivity. The methodology used in the synthesis of the composites was a simple one-pot reaction, combining the simultaneous precipitation of zinc oxide and polycondensation of the resorcinol-based carbon gel. Regarding the composites' characterization, X-ray diffractometry confirms that the composites have the Wurtzite structure of the zinc oxide, whereas the carbon xerogel formation is evidenced by the infrared, diffuse reflectance, and X-ray photoelectron spectroscopies. Morphology-wise, the XC/ZnO is arranged as nodular particle agglomerates, with particles between 500 nm and 50 nm. The photocatalytic tests under simulated solar radiation show that the composites developed are superior to the pure oxide in the photodegradation of sulfamerazine, as all XC/ZnO materials developed achieved higher apparent reaction rate constants (kapp) than pure zinc oxide, with the XC/ZnO 0.5 material obtaining a kapp 75% higher than the one observed for the ZnO sample. Furthermore, the chronoamperometry tests confirmed that the optimized composite (XC/ZnO 0.5) has a greater capacity for photocurrent generation when compared to pure zinc oxide. Therefore, the modification proposed was successful to enhance the photodegradation of sulfamerazine in aqueous media, highlighting the viability of the composites developed for photocatalytic applications.

OPTICAL MATERIALS 128, 112470, 2022. DOI: 10.1016/j.optmat.2022.112470

[P186-2022] "Scintillation light detection in the 6-m drift--length ProtoDUNE Dual Phase liquid argon TPC"

Abud, A. A.; Abi, B.; **Chagas, E. B. das*; Bazetto, M. C. Q.*; Holanda, P. C. de*; Souza, G. de*; Gelli, B.*; Giammaria, P.*; Guzzo, M. M.*; Kemp, E.*; Machado, A. A.*; Peres, O. L. G.*; Pimentel, V. L.*; Prakash, S.*; Segreto, E.***; et al. DUNE Collaboration

DUNE is a dual-site experiment for long-baseline neutrino oscillation studies, neutrino astrophysics and nucleon decay searches. ProtoDUNE Dual Phase (DP) is a 6 x 6 x 6 m(3) liquid argon time-projection-chamber (LArTPC) that recorded cosmic-muon data at the CERN Neutrino Platform in 2019-2020 as a prototype of the DUNE Far Detector. Charged particles propagating through the LArTPC produce ionization and scintillation light. The scintillation light signal in these detectors can provide the trigger for non-beam events. In addition, it adds precise timing capabilities and improves the calorimetry measurements. In ProtoDUNE-DP, scintillation and electroluminescence light produced by cosmic muons in the LArTPC is collected by photomultiplier tubes placed up to 7m away from the ionizing track. In this paper, the ProtoDUNE-DP photon detection system performance is evaluated with a particular focus on the different wavelength shifters, such as PEN and TPB, and the use of Xe-doped LAr, considering its future use in giant LArTPCs. The scintillation light production and propagation processes are analyzed and a comparison of simulation to data is performed, improving understanding of the liquid argon properties.

EUROPEAN PHYSICAL JOURNAL C 82[7], 618, 2022. DOI: 10.1140/epjc/s10052-022-10549-w

[P187-2022] "Search for charged-lepton flavor violation in top quark production and decay in pp collisions at root s=13 TeV"

Tumasyan, A.; Adam, W.; **Chinellato, J. A.*;** et al. CMS Collaboration

Results are presented from a search for charged-lepton flavor violating (CLFV) interactions in top quark production and decay in pp collisions at a center-of-mass energy of 13 TeV. The events are required to contain one oppositely charged electron-muon pair in the final state, along with at least one jet identified as originating from a bottom quark. The data correspond to an integrated luminosity of 138 fb(-1), collected by the CMS experiment at the LHC. This analysis includes both the production (q -> e mu t) and decay (t -> e mu q) modes of the top quark through CLFV interactions, with q referring to a u or c quark. These interactions are parametrized using an effective field theory approach. With no significant excess over the standard model expectation, the results are interpreted in terms of vector-, scalar-, and tensor-like CLFV four-fermion effective interactions.

Finally, observed exclusion limits are set at 95% confidence levels on the respective branching fractions of a top quark to an e mu pair and an up (charm) quark of 0.13 x 10(-6) (1.31 x 10(-6)), 0.07 x 10(-6) (0.89 x 10(-6)), and 0.25 x 10(-6) (2.59 x 10(-6)) for vector, scalar, and tensor CLFV interactions, respectively.

JOURNAL OF HIGH ENERGY PHYSICS [6], 082, 2022. DOI: 10.1007/JHEP06(2022)082

[P188-2022] "Search for invisible decays of the Higgs boson produced via vector boson fusion in proton-proton collisions at root s=13 TeV"

Tumasyan, A.; Adam, W.; **Chinellato, J. A.*;** et al. CMS Collaboration

A search for invisible decays of the Higgs boson produced via vector boson fusion (VBF) has been performed with 101 fb(-1) of proton-proton collisions delivered by the LHC at root s = 13 TeV and collected by the CMS detector in 2017 and 2018. The sensitivity to the VBF production mechanism is enhanced by constructing two analysis categories, one based on missing transverse momentum and a second based on the properties of jets. In addition to control regions with Z and W boson candidate events, a highly populated control region, based on the production of a photon in association with jets, is used to constrain the dominant irreducible background from the invisible decay of a Z boson produced in association with jets. The results of this search arc combined with all previous measurements in the VBF topology, based on data collected in 2012 (at root s = 8 TeV), 2015, and 2016, corresponding to integrated luminosities of 19.7, 2.3, and 36.3 fb(-1), respectively. The observed (expected) upper limit on the invisible branching fraction of the Higgs boson is found to be 0.18 (0.10) at the 95% confidence level, assuming the standard model production cross section. The results are also interpreted in the context of Higgs-portal models.

PHYSICAL REVIEW D 105[9], 092007, 2022. DOI: 10.1103/PhysRevD.105.092007

[P189-2022] "Search for long-lived heavy neutral leptons with displaced vertices in proton-proton collisions at root s=13 TeV"

Tumasyan, A.; Adam, W.; **Chinellato, J. A.***; et al. CMS Collaboration

A search for heavy neutral leptons (HNLs), the right-handed Dirac or Majorana neutrinos, is performed in final states with three charged leptons (electrons or muons) using proton--proton collision data collected by the CMS experiment at root s = 13 TeV at the CERN LHC. The data correspond to an integrated luminosity of 138 fb(-1). The HNLs could be produced through mixing with standard model neutrinos v. For small values of the HNL mass (<20 GeV) and the square of the HNL-v mixing parameter (10(-7)-10(-2)), the decay length of these particles can be large enough so that the secondary vertex of the HNL decay can be resolved with the CMS silicon tracker. The selected final state consists of one lepton emerging from the primary proton-proton collision vertex, and two leptons forming a displaced, secondary vertex. No significant deviations from the standard model expectations are observed, and constraints are obtained on the HNL mass and coupling strength parameters, excluding previously unexplored regions of parameter space in the mass range 1-20 GeV and squared mixing parameter values as low as 10(-7).

JOURNAL OF HIGH ENERGY PHYSICS 7, 081, 2022. DOI: 10.1007/JHEP07(2022)081

[P190-2022] "Search for new physics in the lepton plus missing transverse momentum final state in proton-proton collisions at root s=13 TeV"

Tumasyan, A.; Adam, W.; **Chinellato, J. A.***; et al. CMS Collaboration

A search for physics beyond the standard model (SM) in final states with an electron or muon and missing transverse momentum is presented. The analysis uses data from proton-proton collisions at a centre-of-mass energy of 13 TeV, collected with the CMS detector at the LHC in 2016-2018 and corresponding to an integrated luminosity of 138 fb(-1). No significant deviation from the SM prediction is observed. Model-independent limits are set on the production cross section of W' bosons decaying into lepton-plus-neutrino final states. Within the framework of the sequential standard model, with the combined results from the electron and muon decay channels a W' boson with mass less than 5.7 TeV is excluded at 95% confidence level. Results on a SM precision test, the determination of the oblique electroweak W parameter, are presented using LHC data for the first time. These results together with those from the direct W' resonance search are used to extend existing constraints on composite Higgs scenarios. This is the first experimental exclusion on compositeness parameters using results from LHC data other than Higgs boson measurements.

JOURNAL OF HIGH ENERGY PHYSICS [7], 067, 2022. DOI: 10.1007/JHEP07(2022)067

[P191-2022] "Search for Resonances Decaying to Three W Bosons in Proton-Proton Collisions at ps=13 TeV"

Tumasyan, A.; Adam, W.; **Chinellato, J. A.***; et al. CMS Collaboration

A search for resonances decaying into a W boson and a radion, where the radion decays into two W bosons, is presented. The data analyzed correspond to an integrated luminosity of 138 fb???1 recorded in ffiffiproton-proton collisions with the CMS detector at p s 1/4 13 TeV. One isolated charged lepton is required, together with missing transverse momentum and one or two massive large-radius jets, containing the decay products of either two or one W bosons, respectively. No excess over the background estimation is observed. The results are combined with those from a complementary channel with an all-hadronic final state, described in an accompanying paper. Limits are set on parameters of an extended warped extradimensional model. These searches are the first of their kind at the LHC.

PHYSICAL REVIEW LETTERS 129[2], 021802, 2022. DOI: 10.1103/PhysRevLett.129.021802

[P192-2022] "Search for resonant production of strongly coupled dark matter in proton-proton collisions at 13 TeV"

Tumasyan, A.; Adam, W.; **Chinellato, J. A.*;** et al.
CMS Collaboration

The first collider search for dark matter arising from a strongly coupled hidden sector is presented and uses a data sample corresponding to 138 fb(-1), collected with the CMS detector at the CERN LHC, at root s = 13 TeV. The hidden sector is hypothesized to couple to the standard model (SM) via a heavy leptophobic Z' mediator produced as a resonance in proton--proton collisions. The mediator decay results in two "semi-visible" jets, containing both visible matter and invisible dark matter. The final state therefore includes moderate missing energy aligned with one of the jets, a signature ignored by most dark matter searches. No structure in the dijet transverse mass spectra compatible with the signal is observed.

Assuming the Z' boson has a universal coupling of 0.25 to the SM quarks, an inclusive search, relevant to any model that exhibits this kinematic behavior, excludes mediator masses of 1.5-4.0 TeV at 95% confidence level, depending on the other signal model parameters. To enhance the sensitivity of the search for this particular class of hidden sector models, a boosted decision tree (BDT) is trained using jet substructure variables to distinguish between semivisible jets and SM jets from background processes. When the BDT is employed to identify each jet in the dijet system as semivisible, the mediator mass exclusion increases to 5.1 TeV, for wider ranges of the other signal model parameters. These limits exclude a wide range of strongly coupled hidden sector models for the first time.

JOURNAL OF HIGH ENERGY PHYSICS [6], 156, 2022. DOI: 10.1007/JHEP06(2022)156

[P193-2022] "Shortcuts in Stochastic Systems and Control of Biophysical Processes"

Ilker, E.; Gungor, O.; Kuznets-Speck, B.; Chiel, J.; **Deffner, S.*;** Hinczewski, M.

The biochemical reaction networks that regulate living systems are all stochastic to varying degrees. The resulting randomness affects biological outcomes at multiple scales, from the functional states of single proteins in a cell to the evolutionary trajectory of whole populations. Controlling how the distribution of these outcomes changes over time-via external interventions like time-varying concentrations of chemical species-is a complex challenge. In this work, we show how counterdiabatic (CD) driving, first developed to control quantum systems, provides a versatile tool for steering biological processes. We develop a practical graph-theoretic framework for CD driving in discrete-state continuous-time Markov networks. Though CD driving is limited to target trajectories that are instantaneous stationary states, we show how to generalize the approach to allow for nonstationary targets and local control-where only a subset of system states is targeted. The latter is particularly useful for biological implementations where there may be only a small number of available external control knobs, insufficient for global control. We derive simple graphical criteria for when local versus global control is possible. Finally, we illustrate the formalism with global control of a genetic regulatory switch and local control in chaperone-assisted protein folding. The derived control protocols in the chaperone system closely resemble natural control strategies seen in experimental measurements of heat shock response in yeast and E. coli.

PHYSICAL REVIEW X 12[2], 021048, 2022. DOI: 10.1103/PhysRevX.12.021048

[P194-2022] "Slow crystalline electric field fluctuations in the Kondo lattice SmB6"

Carlone, M.; **Souza, J. C.*;** Sichelschmidt, J.; Rosa, P. F. S.; **Urbano, R. R.*; Pagliuso, P. G.*;** Fisk, Z.; Venegas, P. A.; Schlottmann, P.; **Rettori, C.***

This work reports on the temperature dependence of the electron spin resonance (ESR) of Gd3+-doped SmB6 single crystals at X- and Q-band microwave frequencies in different crystallographic directions. We found an anomalous inhomogeneous broadening of the Gd3+ ESR linewidth (Delta H) within 5.3 K <= T <= 12.0 K which is attributed to slow crystalline electric field (CEF) fluctuations, slower than the timescale of the used ESR microwave frequencies (similar to 10GHz). This linewidth inhomogeneity may be associated to the coupling of the Gd3+S states to the breathing mode of the SmB6 cage and can be simulated by a random distribution of the 4th CEF parameter, b(4), that strikingly takes negative and positive values. The temperature at which this inhomogeneity sets in is related to the onset of a continuous insulator-to-metal phase transition. In addition, based on the interconfigurational fluctuation relaxation model, the observed exponential T dependence of Delta H above T similar or equal to 10 K gives rise to an excitation energy notably close to the hybridization gap of SmB6 (Delta similar or equal to 60 K). This charge fluctuation scenario provides important ingredients to the physical properties of SmB6. We finally discuss the interplay between charge and valence fluctuations under the view of slow CEF fluctuations in SmB6 by coupling the Gd3+ ions to the breathing phonon mode via a dynamic Jahn-Teller-like mechanism.

PHYSICAL REVIEW B 105[20], 205116, 2022. DOI: 10.1103/PhysRevB.105.205116

[P195-2022] "Strain-induced multigap superconductivity in electrene Mo2N: a first principles study"

Pereira, Z. S.; Faccin, G. M.; **Silva, E. Z. da***

Superconductivity in low dimensional materials and 2D electrides are topics of great interest with possible applications in next generation electronic devices. Using density functional theory (DFT) associated with Migdal-Eliashberg approach and maximally localized Wannier functions this study shows how biaxial strain affects superconductivity in a monolayer of Mo2N. Results indicate that 2D Mo2N presents strong electron--phonon coupling with large anisotropy in the superconducting energy gap. It is also proposed that, at low temperatures, a single layer of Mo2N becomes an electride with localized electron gas pockets on the surface, resembling anions adsorbed on an atomic sheet. Calculations point to T-c = 24.7 K, a record high transition temperature for this class of material at ambient pressure. Furthermore, it is shown that when biaxial strain is applied to a superconducting Mo2N monolayer, a new superconductivity gap starts at 2% strain and is enhanced by continuum strain, opening additional coupling channels.

NANOSCALE 14[24], 8594-8600, 2022. DOI: 10.1039/d2nr00395c **(Artigo destaque de capa)**

[P196-2022] "Strategies and performance of the CMS silicon tracker alignment during LHC Run 2"

Tumasyan, A.; Adam, W.; **Chinellato, J. A.*;** et al. CMS Collaboration

The strategies for and the performance of the CMS silicon tracking system alignment during the 2015-2018 data-taking period of the LHC are described. The alignment procedures during and after data taking are explained. Alignment scenarios are also derived for use in the simulation of the detector response. Systematic effects, related to intrinsic symmetries of the alignment task or to external constraints, are discussed and illustrated for different scenarios.

NUCLEAR INSTRUMENTS & METHODS IN PHYSICS RESEARCH SECTION A-ACCELERATORS SPECTROMETERS DETECTORS AND ASSOCIATED EQUIPMENT 1037, 166795, 2022. DOI: 10.1016/j.nima.2022.166795

[P197-2022] "Subthalamic low beta bursts differ in Parkinson's disease phenotypes"

Fim Neto, A.*; Luccas, J. B. de; Bianqueti, B. L.; Silva, L. R. da; Almeida, T. P.; Takahata, A. K.; Teixeira, M. J.; Figueiredo, E. G.; Nasuto, S. J.; Rocha, M. S. G.; Soriano, D. C.; Godinho, F.

Objective: Parkinson's disease (PD) patients may be categorized into tremor-dominant (TD) and postural-instability and gait disorder (PIGD) motor phenotypes, but the dynamical aspects of subthalamic nucleus local field potentials (STN-LFP) and the neural correlates of this phenotypical classification remain unclear.Methods: 35 STN-LFP (20 PIGD and 15 TD) were investigated through continuous wavelet transform and machine--learning-based methods. The beta oscillation - the main band associated with motor impair-ment in PD - dynamics was characterized through beta burst parameters across phenotypes and burst intervals under specific proposed criteria for optimal burst threshold definition.Results: Low-frequency (13-22 Hz) beta burst probability was the best predictor for PD phenotypes (75% accuracy). PIGD patients presented higher average burst duration ($p = 0.018$), while TD patients exhibited higher burst probability ($p = 0.014$). Categorization into shorter and longer than 400 ms bursts led to sig-nificant interaction between burst length categories and the phenotypes ($p < 0.050$) as revealed by mixed-effects models. Long burst durations and short bursts probability positively correlated, respec-tively, with rigidity--bradykinesia ($p = 0.029$) and tremor ($p = 0.038$) scores.Conclusions: Subthalamic low-frequency beta bursts differed between TD and PIGD phenotypes and cor-related with motor symptoms.

CLINICAL NEUROPHYSIOLOGY 140, 45-58, 2022. DOI: 10.1016/j.clinph.2022.05.013

[P198-2022] "Superior in vitro biocompatibility in NbTaTiVZr(O) high-entropy metallic glass coatings for biomedical applications"

Cemin, F.*; Artico, L. L.; Piroli, V.; Yunes, J. A.; Figueroa, C. A.; **Alvarez, F.***

This study combines the brand new concept of high-entropy designed materials with the superior properties of metallic glasses to obtain a NbTaTiVZr high-entropy metallic glass (HEMG) coating for biomedical applications. The amorphous structure is achieved by a room temperature magnetron sputtering deposition, whereas a bcc crystalline phase, typical of high--entropy alloys (HEA), is obtained at 400 degrees C. X-ray photoelectron spectroscopy showed that the oxygen concentration on the coatings surface is > 50% and significantly higher than in the bulk (similar to 5%). The NbTaTiVZr(O) HEMG surface is completely passivated, in contrast to the metallic + oxide outermost layer found for the HEA. Potentiodynamic polarization tests attested an improved corrosion resistance of the HEMG surface, which showed also increased hydrophilicity compared to the crystalline sample. In vitro biocompatibility investigations using both the hTERT-immortalized bone marrow mesenchymal cells and MG-63 osteosarcoma cells showed excellent viability (similar to 98% and similar to 96%, respectively) and adhesion onto the HEMG coating after 96 h of incubation, indicating the integrity and biosafety of this surface. The cell viability and proliferation on the HEA and Ti (used as a benchmark) surfaces were much inferior. The enhanced surface protection and the superior biocompatibility makes the HEMG promising to be employed as a biocoating on orthopedic implants.

APPLIED SURFACE SCIENCE 596, 153615, 2022. DOI: 10.1016/j.apsusc.2022.153615

[P199-2022] "Superparamagnetic and highly bioactive SPIONS/bioactive glass nanocomposite and its potential application in magnetic hyperthermia"

Borges, R.; Ferreira, L. M.; **Rettori, C.*;** Lourenco, I. M.; Seabra, A. B.; Muller, F. A.; Ferraz, E. P.; Marques, M. M.; Miola, M.; Baino, F.; Mamani, J. B.; Gamarra, L. F.; Marchi, J.

Magnetic bioactive glass-ceramics are biomaterials applied for magnetic hyperthermia in bone cancer treatment, thereby treating the bone tumor besides regenerating the damaged bone. However, combining high bioactivity and high saturation magnetization remains a challenge since the thermal treatment step employed to grow magnetic phases is also related to loss of bioactivity. Here, we propose a new nanocomposite made of superparamagnetic iron oxide nanoparticles (SPIONs) dispersed in a sol-gel-derived bioactive glass matrix, which does not need any thermal treatment for crystallization of magnetic phases. The scanning and transmission electron microscopies, X-ray diffraction, and dynamic light scattering results confirm that the SPIONs are actually embedded in a nanosized glass matrix, thus forming a nanocomposite. Magnetic and calorimetric characterizations evidence their proper behavior for hyperthermia applications, besides evidencing inter-magnetic nanoparticle interactions within the nanocomposite. Bioactivity and in vitro characterizations show that such nanocomposites exhibit apatite-forming properties similar to the highly bioactive parent glass, besides being osteoinductive. This methodology is a new alternative to produce magnetic bioactive materials to which the magnetic properties only rely on the quality of the SPIONs used in the synthesis. Thereby, these nanocomposites can be recognized as a new class of bioactive materials for applications in bone cancer treatment by hyperthermia.

BIOMATERIALS ADVANCES 135, 112655, 2022. DOI: 10.1016/j.msec.2022.112655

[P200-2022] "Synthesis and Application of the Ternary Zn0.5Cd0.5S/ZnO/carbon Xerogel Composite in the Photocatalytic Degradation of 4-chlorophenol"

Dantas, G. V. J.; Moraes, N. P. de; Rocha, R. D.; **Siervo, A de***; Lanza, M. R. de V.; Rodrigues, L. A.

The Zn0.5Cd0.5S/ZnO/carbon xerogel photocatalyst was synthesized through the thermal treatment of ZnO, CdS, and a low-cost carbon xerogel matrix at high temperature (600 degrees C). ZnO is one of the most widely used photocatalysts, but it has low visible-light absorption, while Zn0.5Cd0.5S is a visible-light active photocatalyst, which can be used as a co--catalyst to enhance photoactivity under natural radiation and promote charge separation through the creation of Z-scheme heteroj unctions. The further addition of the carbon xerogel can be justified by its highly developed porous structure and ability to capture photogenerated electrons, which will also promote charge separation. The creation of the hexagonal Zn0.5Cd0.5S and ZnO phases was confirmed through the X-ray diffractometry technique. The addition of the carbon xerogel led to an increase in the specific surface area of the XC/ZnO (630%) and XC/ZnO-Zn0.5Cd0.5S (320%) and a decrease in particle size when compared to the pure ZnO. Regarding the photocatalytic performance of the materials, the Zn0.5Cd0.5S/ZnO/carbon xerogel displayed an enhanced photocatalytic activity for 4-chlorophenol degradation, with 84% degradation after 300 minutes of artificial solar irradiation. The enhanced photoactivity of the Zn0.5Cd0.5S/ZnO/carbon xerogel composite was further confirmed by chronoamperometry, as the composite presented higher photocurrent generation under light irradiation.

MATERIALS RESEARCH-IBERO-AMERICAN JOURNAL OF MATERIALS 25, Suplemento 2, e20220038, 2022. DOI: 10.1590/1980-5373-MR-2022-0038

[P201-2022] "Synthesis and Characterization of Biotene: A New 2D Natural Oxide From Biotite"

Mahapatra, P. L.; **Tromer, R.***; Pandey, P.; Costin, G.; Lahiri, B.; Chattopadhyay, K.; Ajayan, P. M.; Roy, A. K.; **Galvao, D. S.*;** Kumbhakar, P.; Tiwary, C. S.

In this work, the synthesis and characterization of ultrathin metal oxide, called biotene, using liquid-phase exfoliation from naturally abundant biotite are demonstrated. The atomically thin biotene is used for energy harvesting using its flexoelectric response under multiple bending. The effective flexoelectric response increases due to the presence of surface charges, and the voltage increases up to approximate to 8 V, with a high mechano-sensitivity of 0.79 V N-1 for normal force. This flexoelectric response is further validated by density functional theory (DFT) simulations. The atomically thin biotene shows an increased response in the magnetic field and thermal heating. The synthesis of two-dimensional (2D) metal--oxide biotene suggests a wealth of future 2D-oxide material for energy generation and energy harvesting applications.

SMALL 18[27], 2201667, 2022. DOI: 10.1002/smll.202201667

[P202-2022] "The stress gradient hypothesis explains plant--plant interaction networks in edapho climatic gradients"

Lima, T. R. A.; Martins, F. R.; Menezes, B. S.; **Marquitti, F. M. D.*;** Sfair, J. C.; Silveira, A. P.; Araujo, F. S.

The stress-gradient hypothesis (SGH) predicts a shift from facilitation to competition as the environment turns from severe to favorable. Different authors have reported conflicting results when testing the SGH, mainly concerning the role of facilitation in stressful environments. We aimed to infer the mechanisms best explaining the variation of interspecific interactions across gradients through the joint analysis of network metrics and abiotic variables. We analyzed six plant-plant interaction networks (size, number of links, connectance, average degree, nestedness, and modularity) in edapho-climatic gradients in northeastern Brazil. Nestedness occurs when many species connect both with each other and with a set of other species with few connections, indicating facilitation. Modularity occurs when the network is split into groups of species linking to each other only within the groups, indicating competition. We used correlation, multiple linear regressions, and a generalized linear model to understand how the abiotic variables could drive network alterations and if the abundance of a possible benefactor species (Fabaceae trees) could increase facilitation. All the climate, soil, and network variables varied widely across the sites. All the sites had aluminium-toxic, nutrient-poor and nitrogen-limited soils, and Hol-dridge's life zones varied from very dry to moist tropical forests. Climate, soil, and network variables were correlated to each other, but the soil was the main driver of variation in the network metrics. Nestedness and modularity were negatively correlated, and both were correlated with the number of Fabaceae trees in each community. Deciduous species in very dry and dry forests require more nitrogen than evergreen species in dry/ moist and moist forests, so the soil was more limiting to the deciduous species, which associated with Fabaceae trees and increased network nestedness. Our data corroborated the SGH, which, in this case, was mediated by the soil nutrient status and had Fabaceae as the benefactor species.

ACTA OECOLOGICA-INTERNATIONAL JOURNAL OF ECOLOGY 115, 103831, 2022. DOI: 10.1016/j.actao.2022.103831

[P203-2022] "Thermal annealing of fission and ion tracks in epidote"

Nakasuga, W. M.*; Li, W. X.; Chen, C. H.; Dumitru, T. A.; Skuratov, V. A.; Ewing, R. C.

Fission tracks are used for geologic age-dating and for the reconstruction of thermal histories of Earth's upper crust. However, there remains a gap in the understanding between the atomic--scale annealing mechanism of latent (unetched) fission tracks and the observations of etched tracks at the micrometer scale. This is because the structure of latent fission tracks is lost during the leaching process. We have conducted the first comparison of the thermal-annealing behavior of latent and etched tracks in epidote, using transmission electron microscopy (TEM) and optical microscopy, respectively. For high-resolution TEM observations, we used ion tracks instead of fission tracks to control the density of tracks, and we demonstrated that latent ion tracks are amorphous in epidote. The reduction in diameters of latent tracks is insignificant after thermal annealing at 800 degrees C for 24 h, indicating that the track diameter does not appear to change substantially until the final stage of annealing. The optical observations show that the parallel etched ion-induced tracks have a lower track density reduction rate at or below 500 degrees C and an accelerated reduction rate above 500 degrees C as compared with randomly oriented fission tracks. However, the two types of tracks display a comparable thermal-annealing behavior as evidenced by the fit of the two curves for the normalized density of ion and fission tracks as a function of temperature with the same equation but with different fitting parameters. Thus, ion-induced tracks can be used to simulate fission tracks in epidote and provide a basis for understanding the annealing of latent and etched tracks.

PHYSICS AND CHEMISTRY OF MINERALS 49[7], 26, 2022. DOI: 10.1007/s00269-022-01200-x

[P204-2022] "Three phases of quantum annealing: Fast, slow, and very slow"

Soriani, A.*; Naze, P.*; Bonanca, M. V. S.*; Gardas, B.; **Deffner, S.***

Currently, existing quantum annealers have proven themselves as viable technology for the first practical applications in the noisy-intermediate-scale-quantum era. However, to fully exploit their capabilities, a comprehensive characterization of their finite-time excitations is instrumental. To this end, we develop a phase diagram for driven Ising chains, from which the scaling behavior of the excess work can be read off as a function of process duration and system size. "Fast" processes are well described by the Kibble-Zurek mechanism; "slow" process are governed by effective Landau-Zener dynamics; and "very slow" processes can be approximated with adiabatic perturbation theory.

PHYSICAL REVIEW A 105[4], 042423, 2022. DOI: 10.1103/PhysRevA.105.042423

[P205-2022] "Unravelling the non-classicality role in Gaussian heat engines"

Oliveira , A. de; **Oliveira, M. C. de***

At the heart of quantum thermodynamics lies a fundamental question about what is genuine "quantum" in quantum heat engines and how to seek this quantumness, so that thermodynamical tasks could be performed more efficiently compared with classical protocols. Here, using the concept of P-representability, we define a function called classicality, which quantifies the degree of non-classicality of bosonic modes. This function allows us to explore the role of non-classicality in quantum heat engines and design optimal protocols for work extraction. For two specific cycles, a quantum Otto and a generalised one, we show that non-classicality is a fundamental resource for performing thermodynamic tasks more efficiently.

SCIENTIFIC REPORTS 12[1], 10412, 2022. DOI: 10.1038/s41598-022-13811-z

[P206-2022] "Unveiling the mechanism of the triethyl phosphate hydrolysis reaction in the synthesis of the sol-gel-derived 58S bioactive glass"

Bueno, O. M. V. M.*; San-Miguel, M. A.; Bertran, C. A.; **Silva, E. Z. da*;** Lopes, J. H.

The sol-gel method is one of the most used methods due to its outstanding capacity to obtain alkaline-earth phosphosilicate bioactive glass with high bioactivity. This efficient synthesis method involves several stages constituted by intermediate chemical reactions, which are governed by mechanisms and kinetic parameters that lead to the formation of the precursor gel of the vitreous matrix. Although the sol-gel method has been widely used for the preparation of materials, some steps are still not completely understood and that affect the final properties of the synthesized materials. For instance, the hydrolysis reaction of triethyl phosphate (TEP) which, similarly to tetraethyl orthosilicate (TEOS), is assumed to be complete in the stage of formation of the precursor gel of the glass matrix. Furthermore, the SN2-type mechanism for the hydrolysis of TEP is widely assumed. However, the absence of studies that support these presumptions fully justifies the use of theoretical methods to gain information about the hydrolysis of TEP within the sol-gel synthesis of 58S bioactive glass. Density functional theory (DFT) and molecular dynamics (MD) simulations were used to study the reaction mechanisms and kinetic behavior of TEP hydrolysis. Our results show that the TEP hydrolysis reaction is very slow in its three stages, occurring not only via the SN(2)mechanism with configuration inversion (SN2-I), as is commonly reported in the literature, but also via SN(2)with configuration retention (SN2-R). Furthermore, it was found that the hydrolysis reaction via SN2-I occurs with faster kinetics than SN2-R. This behavior was observed for the three stages of TEP hydrolysis, both in protonated and non-protonated solutions. Based on our findings on the mechanisms and kinetics of triethyl phosphate hydrolysis reactions, a simple chemical model for the formation of calcium pyrophosphate crystalline domains in 58S sol-gel bioactive glass was proposed. In our model, TEOS undergoes rapid hydrolysis, followed by immediate condensation leading to the formation of three-dimensional silica gels, that permeate non-hydrolyzed TEP molecules due to their slow kinetic rate. This mismatch between the reactions of precursor alkoxides in acidic medium, results in a strong tendency in the formation of a glassy microstructure with low structural homogeneity characterized by crystalline domains of calcium pyrophosphate permeated by a silica-rich glass matrix.

MATERIALS TODAY CHEMISTRY 24, 100929, 2022. DOI: 10.1016/j.mtchem.2022.100929

[P207-2022] "Using Langmuir-Schaefer deposition technique to improve the gas sensing performance of regiorandom polythiophene films"

Oliveira, V. J. R. de; Borro, M. S.; Jesus, L. R. D. do; **Braunger, M. L.*;** Olivati, C. de A.

Polythiophene derivatives are one class of conducting polymers widely tested for application in organic electronics, such as photovoltaic devices, organic light-emitting diodes, and chemosensors to gas and liquid analysis. Polythiophenes can be classified as regioregular or regiorandom, which is determined by the position of their side chains in the polymer backbone, and the regioregular configuration is usually preferred for studies in organic electronic applications. There are few reports in the literature using regiorandom polythiophenes as active layers of devices, all with doped or composite materials. In this context, we have fabricated LangmuirSchaefer films of neutral regiorandom polyalkylthiophenes (P3AT), aiming to evaluate their electrical characteristics compared to the drop-casting technique. The goal was to test whether the Langmuir deposition technique could yield a higher level of organization, while still being mindful of their intrinsic disorder at the molecular level. As a proof-of-concept, the thin films were evaluated as gas sensing devices relying on their resistivity modulation in the presence of ammonia. The devices based on Langmuir-Schaefer films of the regiorandom P3AT showed higher responses to the gas than the ones fabricated by drop-casting, indicating that the organization at the molecular level achieved by the deposition technique improved the gas sensing performance.

SENSORS AND ACTUATORS REPORTS 4, 100094, 2022. DOI: 10.1016/j.snr.2022.100094

[P208-2022] "Using machine learning and an electronic tongue for discriminating saliva samples from oral cavity cancer patients and healthy individuals"

Braz, D. C.; Neto, M. P.; **Shimizu, F. M.***; Sa, A. C.; Lima, R. S.; Gobbi, A. L.; Melendez, M. E.; Arantes, L. M. R. B.; Carvalho, A. L.; Paulovich, F. V.; Oliveira Jr, O. N.

The diagnosis of cancer and other diseases using data from non-specific sensors - such as the electronic tongues (e-tongues) -is challenging owing to the lack of selectivity, in addition to the variability of biological samples. In this study, we demonstrate that impedance data obtained with an e-tongue in saliva samples can be used to diagnose cancer in the mouth. Data taken with a single-response microfluidic e-tongue applied to the saliva of 27 individuals were treated with multidimensional projection techniques and non-supervised and supervised machine learning algorithms. The distinction between healthy individuals and patients with cancer on the floor of mouth or oral cavity could only be made with supervised learning. Accuracy above 80% was obtained for the binary classification (YES or NO for cancer) using a Support Vector Machine (SVM) with radial basis function kernel and Random Forest. In the classification considering the type of cancer, the accuracy dropped to ca. 70%. The accuracy tended to increase when clinical information such as alcohol consumption was used in conjunction with the e-tongue data. With the random forest algorithm, the rules to explain the diagnosis could be identified using the concept of Multidimensional Calibration Space. Since the training of the machine learning algorithms is believed to be more efficient when the data of a larger number of patients are employed, the approach presented here is promising for computer-assisted diagnosis.

TALANTA 243, 123327, 2022. DOI: 10.1016/j.talanta.2022.123327

[P209-2022] "Using the site-knockout strategy to understand the low activity of the nitrate electro-reduction reaction on Pt(111)"

Silva, K. N. da; Soffiati, G.; **Silva, E. Z. da***; San-Miguel, M. A.; Sitta, E.

Nitrate and nitrite reduction reactions (NO3RR and NO2RR, respectively) are important processes in water treatment as well as model processes in surface science. The sluggish kinetics observed for NO3RR on Pt electrodes is usually explained by the difficulty in removing NOad. However, NO2RR shares this same intermediate and depicts higher activity under the same experimental conditions. Herein, we employed the site block strategy to show that the nitrate requires contiguous Pt sites to be converted into nitrite and then to NOad. Both NO3RR and NO2RR were studied on Pt(111) and Pt(111) modified with cyanide ions (Pt(111)-CN). While NO2RR depicted lower activity on Pt(111)-CN than on Pt(111), NO3RR was completely inhibited. Regardless of the presence of cyanide, the DFT-based analysis revealed that both NO3 and NO2 adsorption could occur on the bidentate form.

However, after this step, extra contiguous sites should be provided to ensure NO3ad proceeds with the reduction reaction, which are not available on Pt(111)-CN. These results bring experimental evidence that nitrate to nitrite conversion is an important bottleneck in NO3RR, and the presence of NOad (produced as intermediate during the NO3RR) does not favor this step once NOad also limits the adsorption site size.

NEW JOURNAL OF CHEMISTRY 46[25], 12132-12138, 2022. DOI: 10.1039/d2nj01773c

[P210-2022] "Velocity dispersions of clusters in the Dark Energy Survey Y3 redMaPPer catalogue"

Wetzell, V.; Jeltema, T. E.; Hegland, B.; **Sahlen, M.***; et al. DES Collaboration

We measure the velocity dispersions of clusters of galaxies selected by the red-sequence Matched-filter Probabilistic Percolation (redMaPPer) algorithm in the first three years of data from the Dark Energy Survey (DES), allowing us to probe cluster selection and richness estimation, lambda, in light of cluster dynamics. Our sample consists of 126 clusters with sufficient spectroscopy for individual velocity dispersion estimates. We examine the correlations between cluster velocity dispersion, richness, X-ray temperature, and luminosity, as well as central galaxy velocity offsets. The velocity dispersion--richness relation exhibits a bimodal distribution. The majority of clusters follow scaling relations between velocity dispersion, richness, and X-ray properties similar to those found for previous samples; however, there is a significant population of clusters with velocity dispersions that are high for their richness. These clusters account for roughly 22 per cent of the lambda < 70 systems in our sample, but more than half (55 per cent) of lambda < 70 clusters at z > 0.5. A couple of these systems are hot and X-ray bright as expected for massive clusters with richnesses that appear to have been underestimated, but most appear to have high velocity dispersions for their X-ray properties likely due to line-of-sight structure. These results suggest that projection effects contribute significantly to redMaPPer selection, particularly at higher redshifts and lower richnesses. The redMaPPer determined richnesses for the velocity dispersion outliers are consistent with their X-ray properties, but several are X-ray undetected and deeper data are needed to understand their nature.

MONTHLY NOTICES OF THE ROYAL ASTRONOMICAL SOCIETY 514[4], 4696-4717, 2022. DOI: 10.1093/mnras/stac1623

Errata

Este artigo abaixo, publicado no Boletim Abstracta número 2, de Abril/22 é uma publicação do ano de 2002 e não de 2022 como havia sido indicado.

[E001-2022] "Magnetic relaxation in nanocrystalline systems: linking Monte Carlo steps with time"

Vargas, P.; **Knobel, M.***; Altbir, D.

The magnetic relaxation of a noninteracting two-dimensional ensemble of magnetic nanoparticles is simulated as a function of temperature using a Monte Carlo technique. By properly fitting the decay of magnetization using real parameters it is possible to make, at any finite temperature, a clear correspondence between Monte Carlo steps and time measured in seconds. The results allow one to visualize the intrinsic problems related to the simulation of nonequilibrium systems, and to understand the limits and range of validity of a particular system.

ZEITSCHRIFT FUR METALLKUNDE 93[10], 974-977, 2002. DOI: 10.3139/146.020974

Capítulo de livro

[L001-2022] "Difração de fotoelétrons"

Siervo, A. de*; Lima, L. H. de

SIERVO, Abner de; LIMA, Luis Henrique de. Difração de fotoelétrons. In: PEREIRA, Maria Luiza Rocco Duarte; NASCENTE, Pedro Augusto de Paula (org.). **Técnicas de análise de superfícies**. Rio de Janeiro: Editora Ufrj, 2022. Cap. 6. p. 117-164.

***Autores da comunidade IFGW**
Fonte: Web of Science on-line (WOS)

Defesas de Dissertações do IFGW

[D013-2022] "Imagem por Difração Coerente de Raios-X: Reconstrução de imagem via um modelo matricial da equação de Helmholtz inomogênea"
Aluno: Yuri Rossi Tonin
Orientador: Prof. Dr. Jean Rinkel
Data: 21/07/2022

[D014-2022] "Estudo de espectros PT através da decomposição em polinômios ortogonais"
Aluno: Jhon Mario Cordoba Pareja
Orientador: Profa. Dra. Arlene Cristina Aguilar
Data: 28/07/2022

[D015-2022] "Brillouin Scattering in silica microspheres"
Aluno: Letícia de Sousa Magalhães
Orientador: Prof. Dr. Gustavo Silva Wiederhecker
Data: 28/07/2022

[D016-2022] "Redes Complexas Aplicadas ao Estudo da Difusão de Conhecimento"
Aluno: Vinicius Maciel e Souza
Orientador: Prof. Dr. José Antonio Brum
Data: 19/08/2022

[D017-2022] "Manipulação de Estados do Campo Quantizado Utilizando Meios Lineares e Não-Lineares"
Aluno: Eric Perides Mattos
Orientador: Prof. Dr. Antonio Vidiella Barranco
Data: 19/08/2022

[D018-2022] "Generalized Kuramoto oscillators with external forces"
Aluno: Ana Elisa Dellamatrice Barioni
Orientador: Prof. Dr. Marcus Aloizio Martinez de Aguiar
Data: 26/08/2022

[D019-2022] "Renormalização e escalas em complexos simpliciais"
Aluno: Matheus de Carvalho Loures
Orientador: Prof. Dr. José Antonio Brum
Data: 21/09/2022

Defesas de Teses do IFGW

[T011-2022] "Espectroscopia Raman em óxidos magnéticos com estruturas do tipo perovskita e olivina"
Aluno: Danilo Rigitano Gomes da Silva
Orientador: Prof. Dr. Eduardo Granado Monteiro da Silva
Data: 01/07/2022

[T012-2022] "Investigando as propriedades eletrônicas e ópticas de materiais atomicamente finos com um microscópio de tunelamento com varredura"
Aluno: Ricardo Javier Peña Román
Orientador: Prof. Dr. Luiz Fernando Zagonel
Data: 05/07/2022

[T013-2022] "Modulação acústica da dinâmica excitônica em monocamadas de dicalcogenetos de metais de transição"
Aluno: Diego Scolfaro da Silva
Orientador: Prof. Dr. Odilon Divino Damasceno Couto Junior
Data: 15/07/2022

[T014-2022] "Tratamento perturbativo de processos fora do equilíbrio na cadeia Ising quântica"
Aluno: Artur Soriani Alves
Orientador: Prof. Dr. Marcus Vinicius Segantini Bonança
Data: 11/08/2022

[T015-2022] "Mecânica Computacional de Nanomateriais de Carbono Porosos e Bidimensionais"
Aluno: Levi da Costa Felix
Orientador: Prof. Dr. Douglas Soares Galvão
Data: 12/09/2022

Fonte: Portal IFGW/Pós-graduação - Agenda de Colóquios, Defesas e Seminários.
Disponível em: http://portal.ifi.unicamp.br/pos-graduacao

Cadastre-se como leitor,
e receba os avisos dos novos
números publicados por e-mail.

Abstracta

Instituto de Física
Diretora: Profa. Dra. Mônica Alonso Cotta
Diretor Associado: Prof. Dr. Marcos Cesar de Oliveira
Universidade Estadual de Campinas - UNICAMP
Cidade Universitária Zeferino Vaz
13083-859 - Campinas - SP - Brasil
e-mail: secdir@ifi.unicamp.br
Fone: +55 19 3521-5300

Publicação

Biblioteca do Instituto de Física Gleb Wataghin
http://portal.ifi.unicamp.br/biblioteca
Instagram: @bif.unicamp
Telegram: t.m/bifunicamp

Diretora Técnica: Sandra Maria Carlos Cartaxo
Coordenadora da Comissão de Biblioteca: Profa. Dra. Arlene Cristina Aguilar

Elaboração:
Maria Graciele Trevisan (Bibliotecária)
contato: infobif@ifi.unicamp.br